

Master's Degree Dissertation

Design and Fabrication of Semiconductor Optical Amplifier for High Power Optical Phased Array

(光フェーズドアレイ素子の高出力化に向けた半導体光増幅器の設計と試作)

37-186448 Shota Onozuka

Supervisor : Prof. Yoshiaki Nakano

Department of Electrical Engineering and Information Systems

School of Engineering, The University of Tokyo

January, 2019

Abstract

Light deflection devices are applied to various kinds of fields like imaging, scanning, and remote sensing such as LiDAR. Almost all of those used in LiDAR contain mechanical components that limit steering speed to 1 MHz at most and are vulnerable to vibration, acceleration, and dust. Thus, light deflection devices resistant to vibration, acceleration, and dust and capable of achieving fast steering speed above 10 MHz are required and studied actively for LiDAR applications.

Optical phased arrays (OPAs) are expected as high-speed non-mechanical beam steering devices used for automotive LiDAR applications. While large-scale Si-based OPAs have been demonstrated, the output optical power is restricted by the two-photon absorption effect inside the Si waveguide, which severely limits the maximum measurable distance when used for LiDAR.

In this research, we consider InP-based OPAs with integrated semiconductor optical amplifiers (SOAs), operating at an eye-safe 1550-nm wavelength to achieve high output pulse energy necessary for ToF (time-of-flight) LiDAR applications.

Firstly, We estimated the detection limit energy of the ToF system at the receiver and required optical pulse energy at the emitter. The detection limit energy was derived to be 2.41×10^{-8} nJ with an aperture diameter of 7cm, SNR (Signal-to-Noise Ratio) of 7dB, and an electrical bandwidth of 0.8 GHz. On the other hand, it's estimated at least an optical pulse energy of 44.3 nJ is necessary to reach the ranging distance of 200 m. That means an SOA whose output pulse energy is more than 0.173 nJ is indispensable when the number of OPAs waveguide is 256.

Next, we optimized an epitaxial layer structure of an SOA to get more than 0.173 nJ optical pulse energy by using a numerical model based on the rate equation and then estimated the measurable distance. The results showed that the optical pulse energy within the FWHM (full width at half maximum) of the output pulse was 0.205 nJ and the distance resolution was 19.3 cm. Thus, total output pulse energy is estimated to be 52.4 nJ. As a result, the measurable distance is estimated to be over 200 m, which is a requirement for automotive LiDAR applications.

Finally, We performed the crystal growth to gain conditions for fabricating an epitaxial layer structure we designed.

Table of Contents

Chapter 1 : Introduction	1
1.1 Background.....	1
1.2 Current status of LiDAR and requirements for a long-range LiDAR sensor.....	2
1.3 Solid-state LiDAR	3
Optical Phased Array for LiDAR.....	4
1.4 Ranging technology	6
1.5 Active/Passive Integration	7
1.6 Purpose of this research	9
1.7 Thesis Outline	10
Chapter 2 : Principle	11
2.1 Beam steering method of the OPA.....	11
2.2 Ranging method.....	13
2.3 Phase shift in semiconductor	15
2.4 Semiconductor Optical Amplifier (SOA)	17
Chapter 3 : Design for an SOA integrated into OPAs	19
3.1 Numerical model for the SOA	19
3.2 Solution of rate equations	21
3.3 Signal-to-Noise Ratio (SNR) of an Avalanche Photodiode (APD).....	23
3.4 Analysis and simulation results.....	24
3.4.1 Estimate detection limit energy at the receiver	25
3.4.2 Estimate required optical pulse energy	27
3.4.3 Get some material parameters from experimental results with a reference MQW	29
3.4.4 Optimize the epi layer structure of an SOA for an Offset QW and a Butt-joint method....	32
Chapter 4 : Semiconductor process technology	44
4.1 Deposition process	44
4.2 lithography process	46
4.3 Etching	48
4.4 Crystal growth technology	49
Chapter : 5 Fabrication and measurement.....	50
5.1 Crystal growth for the sample with high compressive strain wells.....	50
5.2 Fabrication of the laser.....	53
5.3 Measurement results of the laser.....	54
5.3.1 Current-Voltage characteristics	54
5.3.2 Optical characteristics.....	55

5.4 Crystal growth for the sample with high optical confinement factor.....	56
Chapter : 6 Conclusion.....	58
6.1 Summary of this research.....	58
6.2 Future issue and prospect.....	59
Appendix A : How to estimate the net Gain from Lasing.....	60
Bibliography	61
List of Publications	64
Acknowledgements.....	65

Chapter 1 : Introduction

1.1 Background

Light deflection devices used to control the direction of laser light are indispensable for a variety of applications using laser light. In those applications, light detection and ranging (LiDAR) is attracting interest in recent years. LiDAR replaces radio waves in radar with laser light and can detect objects at high resolution because of short wavelengths. Besides, it can get information about the distance as radar can do with the ToF method which uses pulse light. In the self-driving system, it's essential to grasp surrounding circumstances three-dimensionally. In addition to LiDAR, millimeter-wave radars and cameras are also used for the ranging, but it's difficult for millimeter-wave to enhance spatial resolution and cameras can't get information about the distance in principle. Thus, LiDAR which can measure the distance at high resolution is said to be indispensable for the self-driving system, and almost all companies including Google adopt it [1]. Except for the self-driving system, LiDAR is used for atmospheric observation making use of scattering by atmospheric aerosols [2].

LiDAR is also used in the field of microscope and biosensing. When it comes to the laser confocal microscope being able to get three-dimensional images at high contrast, it's indispensable to scan laser light and position of samples, and in many cases, laser light is scanned with light deflection devices.

The above contents are applications of OPAs to the light-sensing field. In addition to that field, OPAs are used for photosensitivity of printers, laser processing machines, barcode readers, and various industrial devices. As future potential applications, laser light wireless communication is considered. While the bandwidth of wireless communication is being tight, OPAs are being studied because not only using laser light enables capacities bigger, but also high confidential communication can be performed because of signals never leaked to space[3].

1.2 Current status of LiDAR and requirements for a long-range LiDAR sensor

LiDAR is one of the remote detection and ranging methods that function like radar. It emits infrared light pulses and measures how long the time they take to come back after encountering objects. The time between the emitted laser pulse and the reflected pulse enables the LiDAR sensor to calculate the distance to each object precisely by using the speed of light. LiDAR catches precise distance measurement points at all times, from which 3D information of its surroundings can be obtained. Information about objects' position, shape, and behavior can be gained from this comprehensive mapping of the environment[4].

Mechanical Scanning LiDAR

Mechanical scanning LiDAR is a well-known method for realizing three-dimensional sensing in various applications including site mapping, long-range detection, and high-resolution 360-degree sensing of surroundings. The common component of this type of scanning LiDAR is the use of a highly collimated laser beam that is scanned, often using mirrors or rotation to scan the beam in space[5].

While it can give detailed mapping information of surroundings, it has issues on high price, complexity, and large dimensions which make it unattractive for commercial purposes in automotive applications.

Solid-state LiDAR

Solid-state LiDAR doesn't have mechanical parts and has been said to be the best way for automotive and mobility use solutions. Its benefits with no mechanical components are more cost-efficient to produce than Mechanical Scanning one, which might provide a way to high-volume manufacturing and commercial feasibility, small device size, and high scanning speed due to the no use of mechanical parts.

Requirements for a long-range LiDAR sensor

From Original Equipment Manufacturer (OEM) and Tier 1 perspective, some partly representative requirements are summarized as follows[6]:

- 20 cm distance resolution, 0.1° horizontal, and 0.5° vertical resolution
- 200 m measurement range
- 200\$ system costs
- 20 frames per second of the field of view's point cloud
- 120° horizontal field of view and 16° vertical field of view
- High robustness against shocks and vibrations
- ASIL-C and laser class 1 guaranteeing functional-, eye-, and skin-safety

1.3 Solid-state LiDAR

MEMS LiDAR

MEMS stands for Micro Electro Mechanical Systems. MEMS LiDAR generally uses electromagnetic MEMS mirrors to scan laser light, whose tilt angle varies when applying a stimulus such as a voltage[7].

At this present time, the micro-scanning 1D MEMS mirror concept is the most promising approach towards a long-range (>200m), low-cost (<200\$), robust, and automotive qualified LiDAR system. The 2D MEMS mirror concept can perform not only horizontal scanning but also vertical scanning. However, regarding scanning frequencies, 1D MEMS provides a higher scanning speed than 2D MEMS. The 1D approach normally performs horizontal scanning with a vertical laser beam (Fig. 1.1).

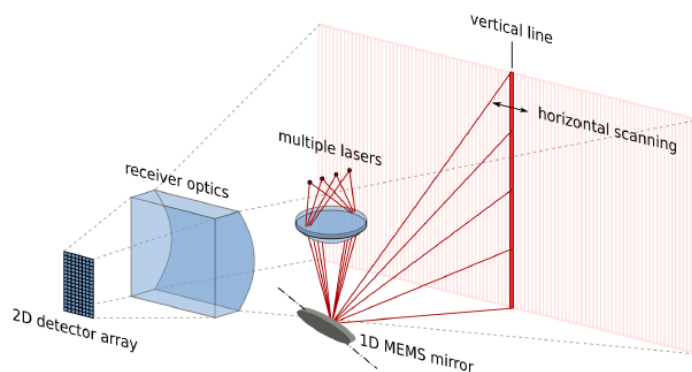


Fig. 1.1 1D micro-scanning LiDAR scanning horizontally with 1D MEMS[6].

Flash LiDAR

Flash LiDAR usually illuminates a scene over a wider field of view by using an expanded laser beam, then gets an image on that scene at a detector array or an imager that can measure the return time of pulses which come from the light source relating to surrounding objects[5].

Flash LiDAR requires different sources depending on applications. Regarding the applications which need a wide field of view, a laser source must have very high peak power such as multiple kW in its narrow pulses (1-10 ns) to meet the required power density to obtain return signals in good condition. On the other hand, regarding the applications which want a narrow field of view to realize long-distance scanning, a laser source must have a peak power around several hundred Watt. These things are shown schematically in Fig. 1.2.

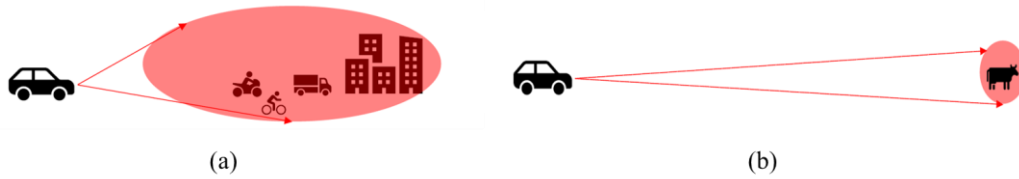


Fig. 1.2 Flash LiDAR applications with different sources[5]: (a) Wide field of view which needs a laser source with very high peak power and large divergence angle. (b) Narrow field of view which needs a laser source with moderate-high peak power and small divergence angle.

To meet the requirements of the narrow field of view Flash LiDAR, Vertical Cavity Surface Emitting Lasers (VCSELs) is considered as one candidate (Fig. 1.3). Additionally, it has merits for the manufacturing and adaptability of integration into electronic packaging.

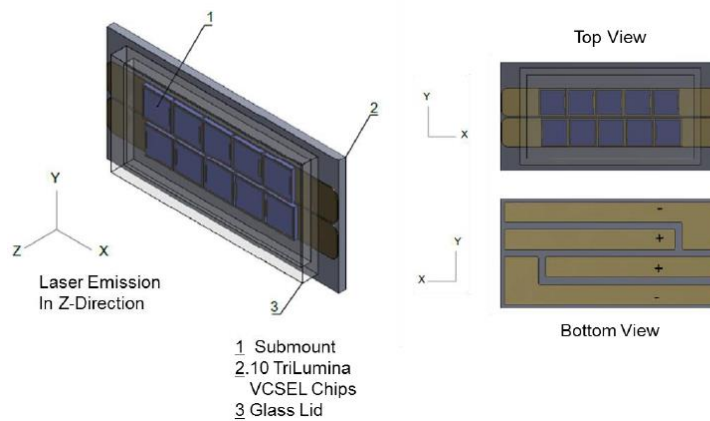


Fig. 1.3 Schematic of VCSELs[5].

Optical Phased Array for LiDAR

Optical Phased Array (OPA) is the device using an optical waveguide structure on materials like semiconductors and just at the principle verification stage now. It is expected as the next generation's light deflection device because of its high potential. In an OPA system, Controlling the speed of light through an optical phase modulator enables control of the optical wavefront shape (Fig. 1.4). The phase of the top beam is not modulated, while the phase of others is modulated to be delayed by increasing amounts such as an electric current. This enables the laser beam steering to point in different directions effectively.

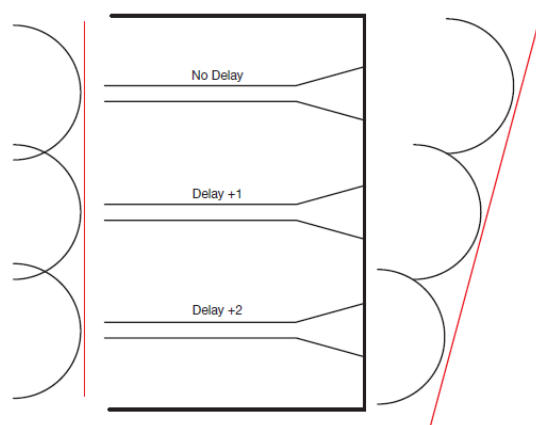


Fig. 1.4 Schematic of the Optical Phased Array (OPA)[7].

As materials, Si and InP are being mainly studied. InP based materials can control the wavelength because of the mixed crystal which can adjust bandgap from $0.92 \mu\text{m}$ to $1.65 \mu\text{m}$. It means InP based materials can be used around $1.3 \mu\text{m}$ and $1.55 \mu\text{m}$ which is the main wavelength for light communication [8]. The big difference between Si and InP based materials is that InP is a direct migration semiconductor which enables to integrate a laser source and semiconductor optical amplifiers (SOAs) monolithically. Furthermore, it has merit for phase modulation because not only the free carrier plasma effect but also the band filling effect happens. That's why modulation efficiency is higher than in Si-based materials.

It is reported that InP based two-dimensional deflection device was realized by W. Guo and his colleagues at the University of California Santa Barbara[9]. The output port of their device is one-dimensional waveguides aligned and uses the diffraction grating to emit light vertically (Fig. 1.5). Phased array method is used for one-dimensional beam steering, and varying the wavelength of light by the diffraction grating is used for the other one-dimensional beam steering. Carrier effects are used for phase modulation, and the response less than $1 \mu\text{s}$ was confirmed. Besides, it succeeded in integrating a tunable laser and SOAs, which demonstrated the superiority of the OPA based on a direct migration semiconductor such as InP.

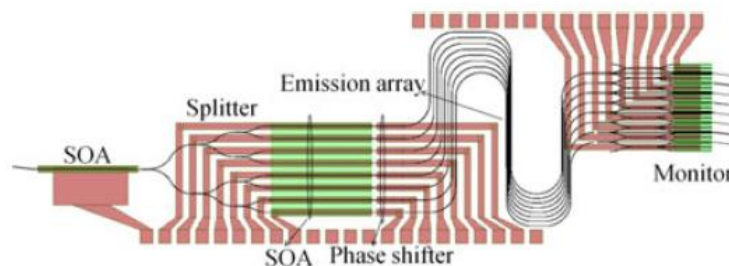


Fig. 1.5 schematic of the two-dimensional deflection device by UCSB[9].

The problems of the Optical Phased Array

Although the OPA has various merits, there are some problems in realizing applications such as LiDAR.

Firstly, there is a problem with the resolution. The beam-width of the OPA is inversely proportional to the number of output waveguides. In other words, resolution points are proportional to the number of waveguides, and they become equal to the number of waveguides. The current LiDAR sensor, for example, the HDL-64E manufactured by Velodyne used in a Google car, has about 6000 resolution points in the horizontal axis, which are more than ten times as much as those demonstrated so far. Due to the integration of semiconductor devices, if the research is conducted with a view to practical applications, it doesn't seem difficult to fabricate the device which has about 1000 resolution points[10].

Secondly, there is a problem in calibration. In the OPA, when the optical path-length changes by several hundred nm, it will affect output. Thus, it's expected the output of the beam doesn't necessarily have the phase as designed due to a variety of fabrication. Furthermore, although it needs to work at a wide temperature range in practical use, temperature-change certainly varies optical path-length, which will affect the output beam. For the above reasons, the fabricated OPA has an arbitrary direction for each temperature. It's necessary to calibrate the input given to each phase shifter so that beam-forming can be performed. The input value that must be set in is proportional to the square of the number of waveguides because resolution points increase in proportion to the number of waveguides. Thus, the larger the device is, the bigger the problem will be.

Finally, there is a problem with output beam power. Although there is no thesis mentioning output power from the fabricated OPA, it's expected output power is less than 1 mW because it seems not to be actively amplified. In order to use a semiconductor element as LiDAR, at least 1W level average output power at eye-safe wavelengths around 1550 nm is said to be necessary[11].

1.4 Ranging technology

Time of Flight (ToF) method

In the ToF method, pulsed light is emitted from the emission part into space, and the light reflected from the object is detected at the light-receiving part. The distance to the object is calculated from the speed of light and the round trip time until light reception. The thing calculated from the round trip time is just the distance, so in order to get three-dimensional information, it's necessary to acquire angle information by beam steering, etc. The distance resolution is dependent on the bandwidth of the light-receiving part, so a relatively fast photodetector is needed. In case the fast enough photodetector can be used, subsequent calculation processing is easy compared with the method using interference because it's possible to calculate the distance directly from the time until light

reception. In addition, there is no restriction associated with coherence length that causes problems when using interference. Therefore, long-distance measurement is also possible.

Frequency modulated continuous wave (FMCW) method

In the FMCW method, sawtooth wave and triangular wave linearly frequency-modulated by a wavelength-tunable laser are emitted into space. At this time, part of the transmitted wave is branched and used as a reference wave. Heterodyne detection is used for the light reflected from objects and acquired at the light-receiving part with the reference wave, and the frequency difference between the two waveforms, which is called beat frequency, is detected. Although the distance to the object is calculated from beat frequency and the rate of frequency change related to time, the bandwidth required for the light-receiving system is narrow due to the small of the beat frequency. Besides, the difference of light path-length between the reference wave and received wave must be shorter than the coherent length of the laser used, so it can be said that it's a suitable ranging method for short-distance measurement.

1.5 Active/Passive Integration

Photonic Integrated Circuit (PIC) consists of active and passive devices, which have different epitaxial structures. To make PIC with active and passive devices, there are some fabrication methods. Common techniques for active/passive integration are butt-joint regrowth[12], offset quantum well[13], dual quantum well[14], and quantum well mixing[13]. Fig. 1.6 shows the cross-sections of each fabrication techniques[12].

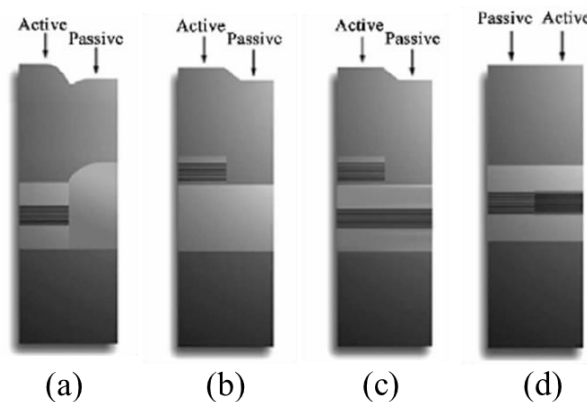


Fig. 1.6 Various methods for active/passive integration[12]: (a) butt-joint regrowth, (b) offset quantum well, (c) dual quantum well, (d) quantum well mixing

In the butt-joint regrowth method, as shown in Fig. 1.6(a), some areas of the epitaxial wafer are etched before growth. After that, an alternative material will be stacked onto the etched areas. The cycle of etching and growth could be iterated. The virtue of this method is being able to do the

growth of optimized structures for different components. The drawback to this method is that it's difficult to achieve high-quality butt-joint interfaces which are concerned with losses and reflections in the core layer.

In the offset quantum well method, as shown in Fig. 1.6(b), a multiple quantum well (MQW) active region is fabricated by etching areas where the gain is not required. The virtues of this method are its simplicity of the fabrication process and low confinement factor in the active MQW which will result in high SOA saturation power theoretically. The drawbacks to this method are it allows for only two band gaps on one chip and the small overlap to an MQW which could be the cause of the inefficiency of active devices. The dual quantum well method as shown in Fig. 1.6(c) is a special version of the offset quantum well method. The offset MQW will be stacked on the bulk waveguide which includes an MQW in the center. In addition to the problems in the offset MQW, high propagation loss in passive waveguides are caused due to the MQW inside core layer.

In the quantum well intermixing method, as shown in Fig. 1.6(d), the longest bandgap wavelength is grown on the wafer in the PIC. After that, the areas where shorter wavelengths are required are exposed to special treatment in order to blur the boundaries of the different MQW by inter-diffusion of elements. This could be performed by ion bombardment, thermal annealing, or high power laser's irradiation. The virtue of this method is the simplicity to implement and more flexibility when compared to the offset quantum well and double quantum well methods. The drawback to this method is the reduction of quantum well quality which will affect some applications[15].

In this research, We consider the offset quantum well and butt-joint regrowth method to integrate active/passive devices on the same chip. These methods are suitable for this particular PIC due to the simplicity of the fabrication process compared to other methods. Cross-section of the schematic of passive and active devices fabricated with the offset quantum well and butt-joint regrowth method is shown in Fig. 1.7.

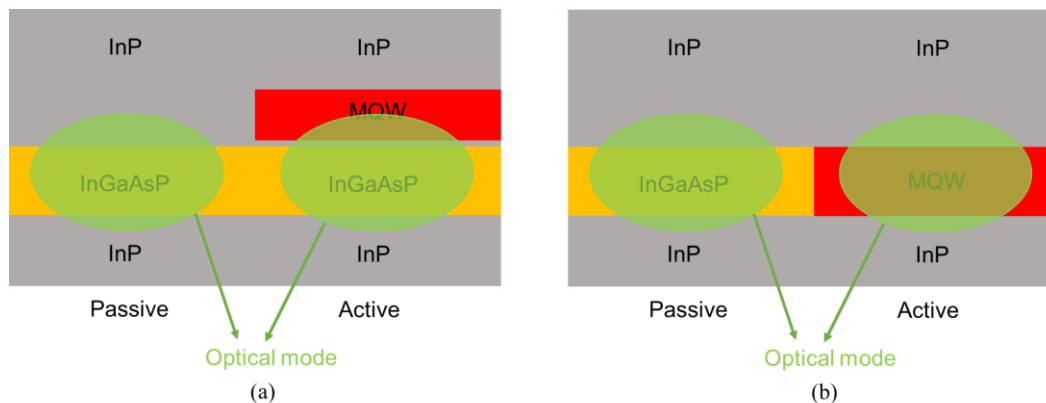


Fig. 1.7 cross-section of the schematic of passive and active InP/InGaAsP photonic devices fabricated with (a) offset quantum well method, (b) butt-joint regrowth method.

1.6 Purpose of this research

The purpose of this research is solving the problems which the OPA has at this present time in order to achieve practical high-speed imaging for some applications such as LiDAR.

In this research, we work on solving the problem especially about the lack of optical output power for LiDAR applications. In order to solve this, SOAs which can realize high optical output power at low optical input power should be integrated into OPA.

Specifically, We estimate the detection limit energy of the ToF system and the required optical output pulse energy of OPAs with SOAs. Then, we optimize an epitaxial layer structure of an SOA to get high optical output pulse energy by using a numerical model based on the rate equation and then estimate the measurable distance.

After that calculation, we perform the crystal growth for my epitaxial layer structure designed through the simulation mentioned above. Besides, we fabricate the all active SOA, active/passive SOA, and OPAs with SOAs to confirm performance. A schematic diagram of the imaging system based on InP integrating a laser monolithically is shown in Fig. 1.8.

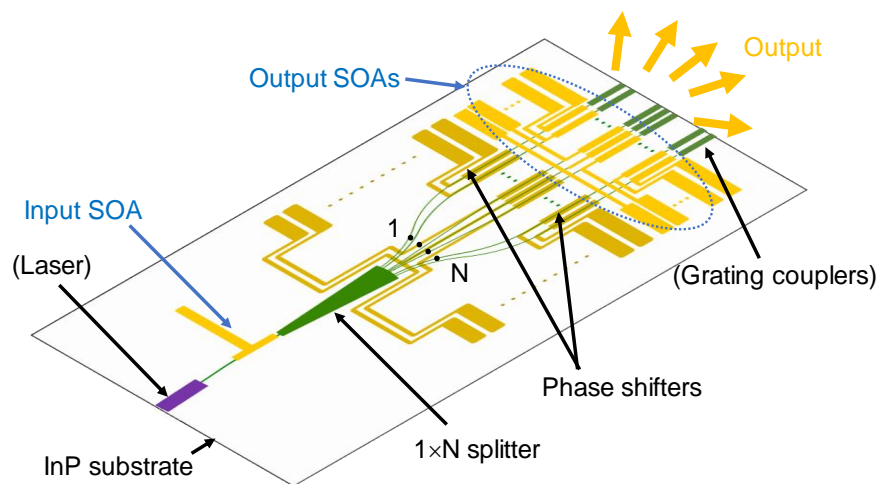


Fig. 1.8 Schematic of the OPA imaging system with SOAs.

1.7 Thesis Outline

This thesis is organized into six chapters as described below.

Chapter 1 introduces the background of this research, the problems of OPAs, and technologies related to OPAs. It also introduces the scope we work on.

Chapter 2 briefly explains the principles of the OPA, SOA, and so on.

Chapter 3 describes the basic physics about gain dynamics of an SOA by using wave propagation equations and carrier rate equations and the SNR equation for incoherent detection with an APD. It also shows the results of the analysis and simulation for optimizing the epitaxial layer structure of an SOA for the high optical pulse energy. Besides, the measurable distance with the optimized SOAs is estimated.

Chapter 4 describes the principles and characteristics of the semiconductor process used to fabricate the SOA and OPA devices.

Chapter 5 describes the fabrication and measurement results of this thesis.

Chapter 6 summarizes our work and make future issue and prospect.

Chapter 2 : Principle

2.1 Beam steering method of the OPA

When the phase is shifted linearly for the output position, the wavefront output from the OPA makes the beam propagating in a specific direction because of diffraction. Lightwave diffraction can be discussed by Fraunhofer diffraction in sufficiently distant regions. As shown in Fig. 2.1, the output direction of the waveguide is z , and the output end is $z = 0$. When defining that the complex amplitudes in the plane of $z = 0$ and Z are $f(x', y')$ and $g(x, y)$, $g(x, y)$ is expressed as follows when Z is sufficiently large[17].

$$g(x, y) = \frac{j}{\lambda Z} \exp(-j \frac{\pi(x^2 + y^2)}{\lambda Z}) \iint_{-\infty}^{\infty} f(x', y') \exp(j 2\pi \frac{xx' + yy'}{\lambda Z}) dx' dy' \quad (2.1)$$

where the plane of $z = 0$ and Z are called the near-field and far-field respectively, and $f(x', y')$ and $g(x, y)$ are called the near-field pattern (NFP) and far-field pattern (FFP). When looking at an integral part of the Eq. (2.1), it's in the form of Fourier transform and when Fourier transformation is defined as below,

$$F(x, y) = \iint_{-\infty}^{\infty} f(x', y') \exp[j 2\pi(xx' + yy')] dx' dy' \quad (2.2)$$

$g(x, y)$ can be written as follows,

$$g(x, y) \propto F(f(x', y'), \left\{ \frac{x'}{\lambda Z}, \frac{y'}{\lambda Z} \right\}) \quad (2.3)$$

where $F(f(x_1), x_2)$ represents Fourier transform for variable x_2 of $f(x_1)$.

We're going to consider the one-dimensional OPA with output waveguides aligned in x' direction for simplicity. Besides, when using $\theta \approx \frac{x}{Z}$, which is the angle seen from the origin, the intensity distribution of FFP is as below.

$$|g(\theta)|^2 \propto \left| \int_{-\infty}^{\infty} f(x') \exp(j \frac{2\pi}{\lambda} \theta x') dx' \right|^2 \quad (2.4)$$

Next, We are going to consider $f(x')$.

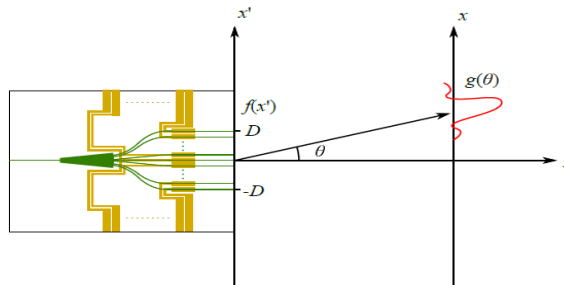


Fig. 2.1 Fraunhofer diffraction.

As shown in Fig. 2.1, the output end of the waveguide is assumed to be placed with sufficiently narrow spacing in the range of $|x'|$. Then, the relative phase $\varphi(x')$ of the waveguide at position x' is assumed to be changed linearly in proportion to tilt γ , which is written as below.

$$\varphi(x') = \gamma x' \quad (2.5).$$

Here, the phase can be folded back by 2π , so a phase shifter only can shift the range of 2π . In this case, $f(x')$ is written as follows.

$$f(x') = \exp(-j\gamma x') \text{rect}(x'/D) \quad (2.6).$$

$$\text{rect}(x) \equiv \begin{cases} 1 & (|x| < 1) \\ 0 & (|x| \geq 1) \end{cases}$$

When substituting Eq. (2.6) into (2.4), the calculation is as follows.

$$|g(\theta)|^2 \propto \left| \int_{-D}^D \exp\left[j\left(\frac{2\pi}{\lambda}\theta - \gamma\right)x'\right] dx' \right|^2$$

$$= \text{sinc}^2\left[\frac{2\pi D}{\lambda}\left(\theta - \frac{\gamma\lambda}{2\pi}\right)\right] \quad (2.7).$$

$$\text{sinc}(x) \equiv \frac{\sin x}{x}$$

FFP will become sinc function centered at $\theta = \frac{\gamma\lambda}{2\pi}$ from Eq. (2.7) and the beam pointing in any direction will be formed by changing γ . Peak gained from Eq. (2.7) is called the main lobe. On the other hand, in fact, waveguides are arranged discretely, and phase distribution on the x' axis is stepped. As a result, high order diffracted light called a grating lobe is generated in $g(\theta)$, and the practically available range of θ is limited. The width of the region where the peak can be moved freely and the grating lobe does not exist is called FSR (free spectral range). In the primary grating lobe, the phase is different by 2π in adjacent waveguides compared to the main lobe. If the spacing of waveguides at the output end is defined as Δd , the necessary γ to shift the phase of the adjacent waveguide by 2π is $\gamma_{2\pi} = 2\pi / \Delta d$. Grating lobe spacing, that is to say, the width of FSR θ_{FSR} which is calculated based on Eq. (2.7) is described as follows.

$$\theta_{FSR} = \frac{\lambda}{\Delta d} \quad (2.8).$$

Besides, Eq. (2.7) shows that the beam width W is inversely proportional to D . Thus, the ratio of FSR to beam width which is resolvable points is as below:

$$\frac{FSR}{W} \propto \frac{\lambda D}{d} \quad (2.9).$$

Since $2D/d$ is the number of waveguide M , resolvable points are about the number of waveguides regardless of the spacing of waveguides.

2.2 Ranging method

Time of flight (ToF) method

The ToF is a distance measurement method that emits pulsed light into space and receives light reflected by an object. Typical ranging set-up is shown in Fig. 2.2. The distance to an object is represented as below.

$$R = \frac{ct_r}{2} \quad (2.10)$$

where R is the distance to an object, c is the speed of light ($c = 3 \times 10^8$ m/s) in the free space, and t_r is the round time between an object and a light receiver. From Eq. (2.10), the attainable resolution in range (ΔR_{\min}), which is directly proportional to the time resolution Δt_r , can be obtained[18]:

$$\Delta R_{\min} = \frac{c\Delta t_r}{2} \quad (2.11).$$

The advantages of the ToF method are its simple device configuration, high depth accuracy, and availability even in dark environments. Thanks to these advantages, this method is the most frequently selected way by manufacturers of imaging LiDAR for the self-driving system. However, this method is limited by the signal to noise ratio (SNR) of the measurement, which requires a minimum SNR of 7 dB[19].

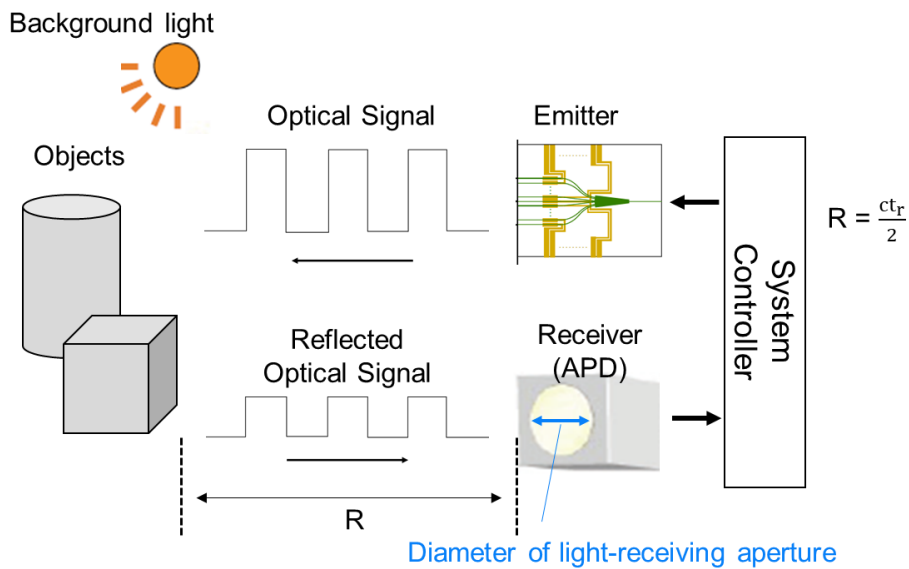


Fig. 2.2 Basic principle of the ToF method.

Frequency modulated continuous wave (FMCW) method

In the FMCW method, the frequency of the emitted light is periodically shifted by varying the source power. The reflected light is blended with the emitted source to create a beat frequency which is used to calculate the distance. A diode laser is typically used as the source to do coherent detection. The distance to an object R is calculated by using a beat frequency f_{beat} as follows[20]:

$$f_{\text{beat}} = \text{slope} \cdot \Delta \tau = \frac{B}{T} t_r = \frac{B}{T} \frac{2R}{c} \quad (2.12)$$

$$R = f_{\text{beat}} \frac{cT}{2B} \quad (2.13)$$

where B is the bandwidth of the frequency, T is the period time of frequency modulation, c is the speed of light ($c = 3 \times 10^8$ m/s) in the free space, $\Delta \tau$ equals to the round time t_r . Fig. 2.3 shows all these parameters. The beat signal in the time domain is transformed to the signal in the frequency domain by using Fast Fourier Transform (FFT), and the peak of beat frequency is translated easily

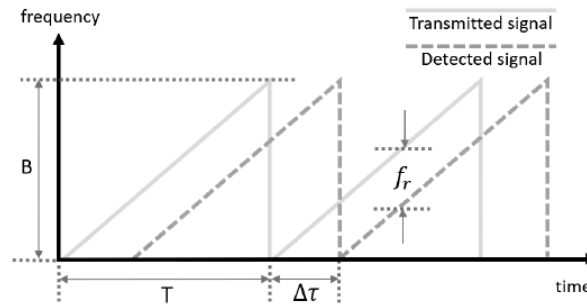


Fig. 2.3 Basic principle of the FMCW method[20]: main parameters.

into the distance.

In this method, triangular frequency modulation is typically used (Fig. 2.4) rather than a sawtooth wave. The frequency of the modulation, in this case, is represented as f_m . Therefore, the rate of changing frequency can be written as $2f_m B$, and the beat frequency is given by the below equation.

$$f_{\text{beat}} = \frac{4Rf_{\text{beat}}B}{c} \quad (2.14)$$

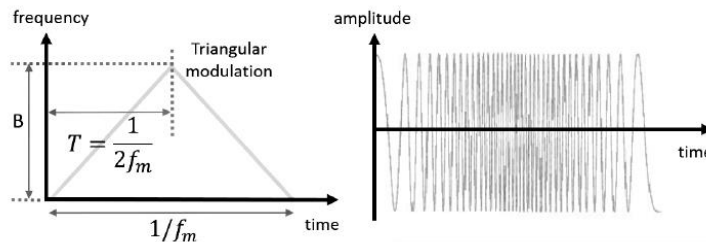


Fig. 2.4 Triangular frequency modulation with time and linked amplitude signal change[20]

2.3 Phase shift in semiconductor

Phase shifters necessary to realize OPAs method based on the Semiconductor change refractive index by using various optical effects caused in waveguides. The change in the refractive index is linked with the change in the absorption rate which is associated with Kramers-Kronig relation, and the change in the absorption rate is caused by the change in the bandgap. In this thesis, we introduce the effects mainly contributing to the phase shift of OPAs based on the semiconductor.

Thermo-optic effect

The thermo-optic effect is a phenomenon in which the refractive index increases due to the increase of temperature in the medium, and is caused by the increase of lattice constant of the crystal. Fig. 2.5 shows an example of the relationship between the interatomic potential in the crystal and the interatomic distance. In the region where the distance is short, the potential increases rapidly due to Pauli's exclusion law, whereas in the region where the distance is large, if more energy than the binding energy is given to an atom, it can jump to infinity. Therefore, if energy is given to atoms within this potential, it can be seen the average distance between atoms increases. This is the physical origin of thermal expansion and the lattice constant increases as temperature increases. Since the bandgap is caused by the interaction of atoms in the crystal, the smaller the lattice constant is, the bigger the bandgap is. As a result, materials with a small atomic number, such as diamond, have a large bandgap, whereas those with a large atomic number have a small bandgap. Since lattice constant becomes larger due to temperature rise, the bandgap becomes smaller and the reflective index increases because of Kramers-Kronig relations. As the equation describing the temperature dependence of the bandgap E_g , the empirical formula by Varshni is known[21] :

$$E_g(T) = E_g(0) - \frac{\alpha T^2}{T + \beta} \quad (2.15)$$

where T is absolute temperature, α and β are fitting parameters. Some values of the parameters in Varshni's equation are shown in Table. 2.1.

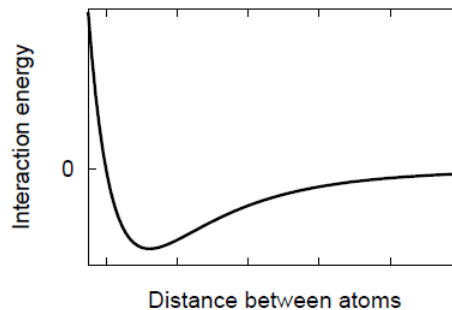


Fig. 2.5 Potential energy between two atoms.

Table. 2.1: Values of the parameters in Varshni's equation [21].

Material	$E_g(0)$ [eV]	α [$\times 10^{-4}\text{K}^{-1}$]	β [K]
Si	1.1557	7.021	1108
GaAs	1.5216	8.871	572
InP	1.4206	4.906	327

Carrier effects

The carrier effect is a general term for refractive index changes caused by changes in the carrier density in a semiconductor, including band-filling effect, free carrier effect, and bandgap shrinkage effect[22].

- Band-filling effect

When carriers are injected into a semiconductor, the level at the bottom of the conduction band is filled with carriers. This makes the energy gap broadened between levels that can transit from the valence band, and an effective bandgap becomes large. This corresponds to the shift of the absorption edge to the short wavelength side, and changes in the refractive index get $\Delta n < 0$ as the absorption coefficient decreases.

- Bandgap shrinkage effect

When electrons injected into the semiconductor fill the bottom of the conduction band, the electrons repel each other due to the Coulomb force, and the energy is lowered to fill the level so that the spins do not face in the same direction. Doing this lowers the lower end of the conduction band, and raises the upper end of the valence band by the same phenomenon in holes. The bandgap contracts due to both fluctuations, and the absorption edge shifts to the long wavelength. As a result, the absorption coefficient gets bigger and changes in the refractive index get $\Delta n > 0$.

- Free carrier effect

Free carriers in the band also absorb light and transit to a higher level. As a result, changes in the refractive index get $\Delta n < 0$.

The calculation result of the refractive index change due to carrier effects on InP is shown in Fig. 2.4. In the band filling effect and bandgap shrinkage effect, the refractive index spectrum changes greatly near the bandgap since the absorption spectrum changes greatly near bandgap. On the other hand, in the free-carrier effect which is not so much dependent on the absorption spectrum, the spectrum of the refractive index change is flat. As the carrier increases, the bandgap shrinkage effect

increases the refractive index. On the other hand, the band-filling effect and free-carrier effect decreases it. As a total, latter effects become dominant so that the refractive index decreases.

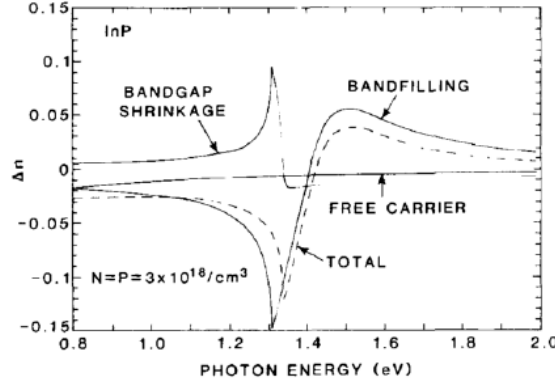


Fig. 2.6 Calculation result of the refractive index change on InP caused by carrier effects[22]. Electron and hole densities are $3 \times 10^8 \text{ cm}^{-3}$. Bandgap energy of InP is 1.34 eV.

When it comes to the phase shift caused by carrier effects, There are two methods. One is injecting current into double heterostructure in order to fill the lower end of the conduction band with electrons and the upper end of the valence band with holes. The other is pulling out carriers by applying a reverse bias voltage.

2.4 Semiconductor Optical Amplifier (SOA)

Fig. 2.7 shows the typical structure of the SOA. SOA typically has optical waveguide and optical gain mechanism formed on a compound semiconductor such as InP and GaAs. The signal light into the input end face is converted into a certain guided mode by the optical waveguide and propagates in the device. The optical gain mechanism is arranged to affect the optical field distribution in this guided mode, and inverted population and stimulated emission formed by current injection into the semiconductor active layer causes optical gain[23]. Thus, the signal light propagating in the element feels optical gain and that intensity is amplified while propagating toward output end.

The steady-state performance of the SOA is written by some factors. The main factors deciding the output power of an SOA are the small-signal gain (G_s) and saturation output power ($P_{o,sat}$). The small-signal gain can be represented as follows [16]:

$$G_s = \exp[(\Gamma g - \alpha_i)L] \quad (2.16)$$

where L is the length of the SOA, Γ is the optical confinement factor of the active layer, g is the unsaturated active-material gain coefficient, α_i is the internal loss coefficient. During the amplification process, the carriers in the active gain region decrease when the optical power increases, decreasing amplifier gain G to half of the small-signal gain and resulting in the power saturation. The saturation output power can be written as:

$$P_{o,sat} = \left(\frac{G_s \ln 2}{G_s - 2} \right) A \left(\frac{h\nu}{a\tau} \right) \quad (2.17)$$

where $h\nu$ is the photon energy, a is the differential gain, τ is the carrier lifetime, G_s is the unsaturated gain, and A is the cross-sectional area of the active layer where the light passes. In a typical SOA, A can be described as:

$$A = \frac{WD}{\Gamma} \quad (2.18)$$

where D and W are the thickness and width of the active material. $P_{o,sat}$ is proportional to the cross-sectional area of the active layer where the light passes, and inversely proportional to the optical confinement factor of the active layer. These parameters can be adjusted to increase $P_{o,sat}$ by the proper design of the waveguide structure.

The noise figure (NF) of an SOA is represented like

$$NF = \frac{1}{\eta_{c,in}} \frac{2n_{sp}(G-1)}{G} \frac{\Gamma g}{\Gamma g - \alpha_i} + \frac{1}{\eta_{c,in}\eta_{c,out}G} \quad (2.19)$$

Where $\eta_{c,in}(\eta_{c,out})$ is the input (output) coupling efficiency, g is the saturated material gain, and n_{sp} is the population inversion factor.

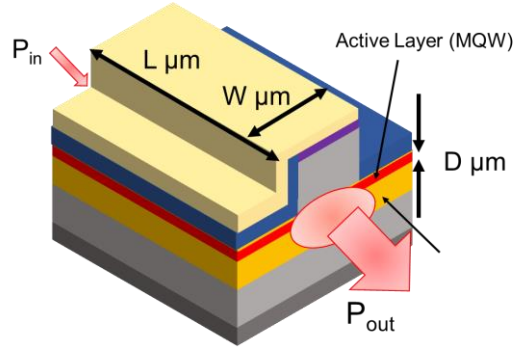


Fig. 2.7 Schematic of the Semiconductor Optical Amplifier.

Chapter 3 : Design for an SOA integrated into OPAs

In this chapter, we will firstly explain the numerical model used for the simulation, and then show results of the analysis and simulation optimizing an epitaxial layer structure for the SOA.

3.1 Numerical model for the SOA

An SOA properties can be calculated based on the carrier rate equation and wave propagation equation[24].

Carrier rate equation

The carrier rate equation can describe how an optical output is affected by injecting current. The densities of electrons equal those of holes due to charge neutrality, so we only track densities of electrons for simplicity. We use $n(x, y, z, t)$ for representing densities of electrons inside the SOA. When neglecting the carrier diffusion due to uniform distribution of electrons, the carrier rate equation for electrons can be expressed as below:

$$\frac{dn(t)}{dt} = \frac{I}{qV} - R_{nonrad} - R_{st} \quad (3.1)$$

where I is current, q is the elementary charge, and V is the volume of the active region. The first term in the right part of Eq. (3.1) is carrier generation rate and means electrons injected into the active region per unit volume and second. The others in the right part of Eq. (3.1) are recombination rates. The second term represents non-stimulated carrier decay processes. It can be written as:

$$R_{nonrad} = An + Bn^2 + Cn^3 \quad (3.2)$$

where A, B, C is called the nonradiative recombination coefficient, the bimolecular recombination coefficient, and the Auger recombination coefficient respectively.

The third term is the stimulated emission rate, representing the gain process of photons. We define g as the incremental gain per unit length Δz and n_p as the photon density increasing after passing through the gain medium:

$$n_p(z + \Delta z) = n_p(z)e^{g\Delta z} \quad (3.3)$$

The stimulated emission term can be rewritten as below using the proximity relation of the exponential function, $e^{g\Delta z} \approx 1 + g\Delta z$.

$$\left(\frac{dn_p}{dt}\right)_{gen} = R_{st} = v_g g n_p \quad (3.4)$$

where v_g is the group velocity. From the content mentioned above, Eq. (3.1) can be expressed as[25]:

$$\frac{dn}{dt} = \frac{I}{qV} - (An + Bn^2 + Cn^3) - v_g g n_p \quad (3.5)$$

Traveling wave equation

Traveling wave equation derived from the Maxwell equation can represent the propagation of the electromagnetic field inside the SOA. The wave equation for the counter-propagating signal field is expressed as[26]:

$$\pm \frac{\partial E^\pm(z,t)}{\partial z} + \frac{1}{v_g} \frac{\partial E^\pm(z,t)}{\partial t} = \frac{1}{2}(\Gamma g - \alpha_i)E^\pm(z,t) + j\Gamma k_0 \Delta n E^\pm(z,t) \quad (3.6)$$

where $E(z,t)$ is the electrical field of the optical signal, k_0 is the wavenumber, Δn is the change in the refractive index caused by current injection, Γ is the confinement factor, α_i is the internal loss, $-$ represents the backward propagating wave, and $+$ means the forward propagating wave. Usually, the electric field of the optical signal can be separated into optical power $P(z,t)$ and phase $\varphi(z,t)$:

$$E(z,t) = \sqrt{P(z,t)}e^{-j\varphi(z,t)} \quad (3.7)$$

When substituting Eq. (3.7) into Eq. (3.6), the wave equation becomes

$$\pm \frac{\partial P^\pm(z,t)}{\partial z} + \frac{1}{v_g} \frac{\partial P^\pm(z,t)}{\partial t} = (\Gamma g - \alpha_i)P^\pm(z,t) \quad (3.8)$$

$$\pm \frac{\partial \varphi(z,t)}{\partial z} + \frac{1}{v_g} \frac{\partial \varphi(z,t)}{\partial t} = -\frac{\Gamma k_0 \Delta n}{\varphi} \quad (3.9).$$

Furthermore, the power of spontaneous emission in the ASE field can be described by using the wave equation:

$$\pm \frac{\partial \rho_{ASE}^\pm(z,t)}{\partial z} = (\Gamma g - \alpha_i)\rho_{ASE}^\pm(z,t) + \rho_{spont}(z,t) \quad (3.10)$$

where ρ_{spont} is the spontaneous emission power spectral density, and ρ_{ASE}^\pm is the amplified spontaneous emission power spectral density propagating forward and backward.

Gain equation

Material gain is known to be expressed as a linear function of carrier density in laser theory as below[25]:

$$g(n(z,t)) = a_0(n(z,t) - n_0) \quad (3.11)$$

where n_0 is the carrier density at transparency, and a_0 is the differential gain coefficient. When taking the strong saturation effect caused by the co-existence of forward and backward propagating waves in the SOA due to the existence of reflectivity on the facets into consideration, Eq. (3.11) can be modified as bellows[27]:

$$g^+(z,t) = \frac{a_0(n-n_0)}{1+\varepsilon_{11}n_p^+ + \varepsilon_{12}n_p^-} \quad (3.12)$$

$$g^-(z,t) = \frac{a_0(n-n_0)}{1+\varepsilon_{22}n_p^- + \varepsilon_{21}n_p^+} \quad (3.13)$$

Where g^+ and g^- are the modified material gain for forward and backward propagation respectively. ε_{11} and ε_{22} are the self-gain saturation coefficients. ε_{12} and ε_{21} are the cross-gain saturation coefficients. The cross-gain saturation coefficients are always double of self-gain saturation coefficients[27].

3.2 Solution of rate equations

We apply the finite difference method to solve the carrier rate equations for calculating SOA's characteristics. Fig. 3.1 shows the SOA model. In this model, we slice the device into m spatial sections. When the length of each section is short enough, it is possible considering that gain and carrier density is constant in each section. However, the value of carrier density varies due to wave propagation. Not only Signal but also ASE are included in the propagating optical field. ASE affects the performance of the SOA, especially at low stimulated emission.

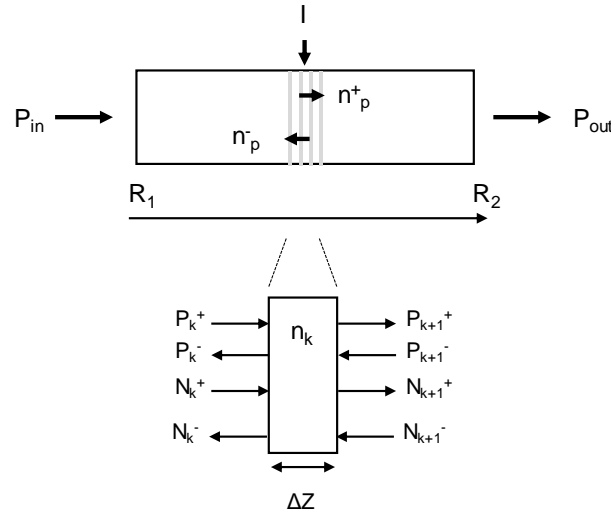


Fig. 3.1 Schematics of SOA model

We firstly apply the finite difference method to Eq. (3.5). The term in the left part of that equation can be written otherwise by using the difference of carrier density n between the current time and next time slot:

$$\frac{dn(z,t)}{dt} = \frac{n(z,t+\Delta t) - n(z,t)}{\Delta t} = \frac{n_k(t+\Delta t) - n_k(t)}{\Delta t} \quad (3.14).$$

Subscript k is used to express the k th section. When substituting Eq. (3.14) into Eq. (3.5), we have the below recurrence equation,

$$n_k(t + \Delta t) = n_k(t) + \Delta t \left[\frac{I(t)}{qV} - R(n_k) - v_g g_k^+ (n_{p,k}^+ + n_{ase,k}^+) - v_g g_k^- (n_p^- + n_{ase}^-) \right] \quad (3.15).$$

Carrier density in the kth section at the next time can be calculated using the above equation. Besides, the carrier density in the (k+1)th section is similarly calculated with the data about the value of gain, injected current, carrier density, and photon density at last time.

It's difficult to get the recurrence relation of Eq. (3.8) only with the finite difference method used. Thus, we need to make it simple with the transformation of the formula like below[28]

$$\tau = t - \frac{z}{v_g} \quad (3.16).$$

By using the above formula, the solutions of Eq. (3.8) are derived as

$$P_{k\pm 1}^{\pm}(t + \Delta t) = P_k^{\pm} e^{(\Gamma g_k^{\pm}(t) - \alpha)\Delta z} \quad (3.17).$$

The above equation represents the relationship of adjacent optical signal powers, which means the power in the (k±1)th segment can be gained with the information in the kth section. Optical power in the (k±2)th segment can also be calculated using the information in the (k±1)th segment as well.

When it comes to ASE noise propagation, it's effective to make use of the finite difference method like what we did to the carrier rate equation. The forward propagating ASE can be expressed as below by only taking the forward differential part of Eq. (3.10) into consideration,

$$\rho_{ase,k+1}^+ = [1 + (\Gamma g_k^+ - \alpha)\Delta z]\rho_{ase,k}^+ + \rho_{spont,k}\Delta z \quad (3.18).$$

Since Δz is small enough, the first term in the right part can be expressed as the exponential term by using

$$e^z \cong (1 + z) \quad (3.19).$$

Thus, Eq. (3.18) is written as

$$\rho_{ase,k+1}^+ = e^{(\Gamma g_k^+ - \alpha)\Delta z}\rho_{ase,k}^+ + \rho_{spont,k}\Delta z \quad (3.20).$$

Eq. (3.20) means the ASE power occurs due to two causes in each segment. One cause is the amplified input noise which experiences the same process as signal propagation, and the other cause is the spontaneous emission component in that segment. In a segment of length Δz , the power density of generated spontaneous emission in that segment is given by [29]:

$$\rho_{spont,k}\Delta z = f_{sp}(G_k - 1)h\nu \quad (3.21).$$

Where G_k represents the signal gain in the kth segment, which is equal to $e^{(\Gamma g_k^+ - \alpha)\Delta z}$, and f_{sp} represents the spontaneous emission factor. In this model, given a constant noise power spectral density on an optical bandwidth B_0 , the recurrence relationships of ASE power can be described as,

$$P_{ask,k\pm 1}^{\pm} = P_{ask,k}^{\pm} e^{(\Gamma g_k^{\pm} - \alpha)\Delta z} + f_{sp} \left(e^{(\Gamma g_k^{\pm} - \alpha)\Delta z} - 1 \right) h\nu B_0 \quad (3.22).$$

The boundary conditions in this model are:

$$P_0^+ = R_1 P_0^- + (1 - R_1) P_{in} \quad (3.23)$$

$$P_m^- = R_2 P_m^+ \quad (3.24)$$

$$N_0^- = R_1 N_0^- \quad (3.25)$$

$$N_m^- = R_2 N_m^+ \quad (3.26)$$

Where P_{in} is input optical power, R_1 and R_2 are the reflection coefficient of front and rear facet, and m means the SOA is divided into m sections.

The output signal power and ASE power are,

$$P_{out}(t) = (1 - R_2)P_m^+ \quad (3.27)$$

$$N_{out}(t) = (1 - R_2)N_m^+ \quad (3.28).$$

3.3 Signal-to-Noise Ratio (SNR) of an Avalanche Photodiode (APD)

The SNR equation for amplified direct detection by an APD is expressed as[30]

$$SNR_{APD} = \frac{P_{sig}}{P_{th} + P_a + P_{dark} + P_{shot} + P_{back}} \quad (3.29)$$

where P_{sig} is the return signal power at the receiver, P_{th} is the thermal noise power, P_a is the electronic amplifier noise, which are unaffected by the APD, P_{dark} is the dark current noise at the receiver, P_{shot} is the quantum shot-noise power, and P_{back} is the background illumination shot noise power.

3.3.1 Return signal power

The return signal power at the receiver with an APD is written by

$$P_{sig} = I^2 R_L = (M \varphi_r \chi)^2 R_L \quad (3.30)$$

where I is the photocurrent detected at the receiver, R_L is the load resistance, M is the signal gain of the APD, φ_r is the detected optical power, and χ is the detector's responsivity ($\chi = \eta q / h\nu$), where η is the quantum efficiency of the receiver, q is the electron charge value, h is Plank's constant, and ν is the light frequency.

3.3.2 Thermal noise

The thermal noise power is expressed as

$$P_{th} = 4kTB \quad (3.31)$$

where k is Boltzmann's constant, T is temperature, and B is electrical bandwidth ($1/2\Delta t$, where Δt is the pulse width in time region).

3.3.3 Electronic amplifier noise

The electron amplifier noise is represented as

$$P_a = 4kT_a B \quad (3.32)$$

where T_a is the temperature of effective noise which is expressed as $T_a = T(NF - 1)$, where NF is the amplifier noise figure.

3.3.4 Quantum shot-noise

The quantum shot-noise depends on the photocurrent detected at the receiver and is written for amplified direct detection like

$$P_{shot,APD} = 2q\varphi_r\chi M^2 F_{ex} BR_L \quad (3.33)$$

where F_{ex} is an excess noise factor.

3.3.5 Dark current noise

The dark current noise at the receiver is written as

$$P_{dark,APD} = 2q\varphi I_{dark} M^2 F_{ex} BR_L \quad (3.34).$$

3.3.6 Background noise

The background noise at the receiver can be represented like

$$P_{back,APD} = 2q\varphi_B \chi M^2 F_{ex} BR_L \quad (3.35)$$

where φ_B , the received background power of the solar irradiance impinging on the detector, is given by

$$\varphi_B = S_{IRR} \Delta\lambda \Omega_R \rho_B \varepsilon_{opt} A_R \quad (3.36)$$

and S_{IRR} is the solar irradiance at the Earth, $\Delta\lambda$ is the optical bandwidth of the receiver, Ω_R is the incident solid angle, ρ_B is the background reflectivity, ε_{opt} is the optical receiver efficiency, and A_R is the receiver aperture area.

3.3.7 Signal to noise ratio of an APD

We could get the overall electronic SNR for direct detection with an APD by substituting Eq. (3.30)-(3.36) into Eq. (3.29), which is written as follows

$$SNR_{APD} = \frac{\varphi_r^2 \chi^2 R_L M^2}{4k_B(T+T_a) + 2qM^2 F_{ex} BR_L (\varphi_r \chi + \varphi_B \chi + I_{dark})} \quad (3.37).$$

3.4 Analysis and simulation results

In order to achieve more than 200m ranging distance by the OPAs integrated with SOAs, we firstly estimated the detection limit energy and required optical pulse energy by calculating the relationship between optical pulse energy and ranging distance at some diameters of light-receiving aperture. The detection limit energy can be decided from the relationship between signal gain of the APD and detection limit energy.

Next, we optimized the epitaxial layer structure of an SOA by numerical analysis and then examined the applicability to the ToF LIDAR by estimating optical pulse energy in an offset quantum well method and a butt-joint method respectively.

3.4.1 Estimate detection limit energy at the receiver

The detection limit energy at the receiver is restricted by noises explained in chapter 3.3. Besides, it's known that a minimum SNR of 7 dB is required for ranging [19].

We firstly estimated values of noises to calculate SNR and to find proper diameter of the aperture with a various signal gain of an APD. Fig. 3.2 shows calculation results and Table. 3.1 shows the values of the parameters in this simulation.

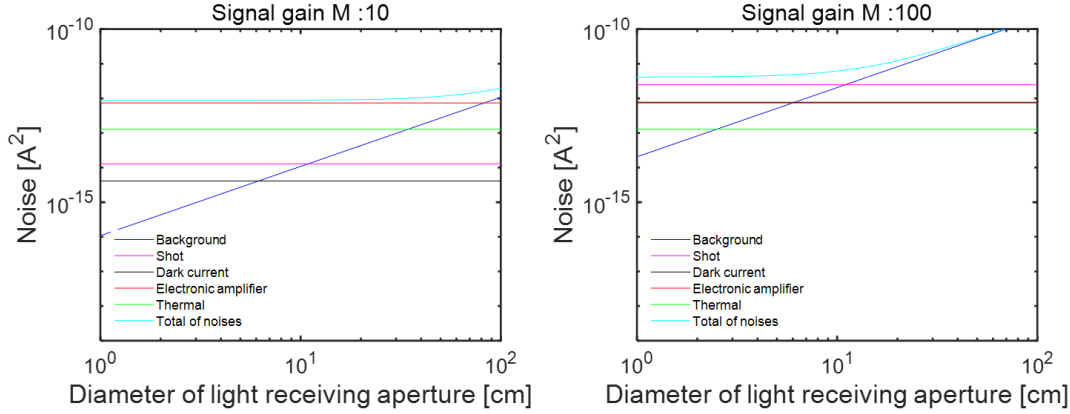


Fig. 3.2 Diameter of light receiving aperture versus each value of noises when signal gain of the APD is 10 and 100

Table. 3.1: Values of the parameters in the noise calculation

Parameter	Symbol	Value
Wavelength	λ	1550 nm
Electrical bandwidth	B	0.8 GHz
Resolution		19 cm
Speed of light	c	3×10^8 m/s
Capacitance	C	1.96 pF
Resistance	R	102.8 Ω
Boltzmann constant	k	1.38×10^{-23} m ² kg ⁻² K ⁻¹
Absolute temperature	T	300 K
Effective noise temperature	T_a	1728 K
Noise figure	NF	6.76
Material gain*	g	2000 cm ⁻¹
Waveguide loss †	a_i	15 cm ⁻¹
Optical confinement factor*	Γ	61.90%
Population inversion factor	n_{sp}	1
Input (output) coupling efficiency	$\eta_{c.in}(\eta_{c.out})$	0.3
Small signal gain*	G_0	631
Quantum efficiency	n	0.8
Elementary charge	q	1.6×10^{-19} C
Planck constant	h	6.63×10^{-34} m ² kg/s
Return signal power	P_{sig}	-35 dBm
APD gain	M	10~100
Excess noise figure	F	1.62~3.08
Dark current	I_{dark}	100 nA
Solar irradiance at the Earth	S_{IRR}	0.266 W / (m ² nm sr)
Background reflectivity	ρ_B	5%
Optical bandwidth	$\Delta \lambda$	0.25 nm
optical receiver efficiency	ϵ_{opt}	0.65
Incident solid angle	Ω_R	0.0123 sr
Diameter of light receiving aperture	d	1~100 cm

* Derived by simulation, † Fitted to experimental results

When the diameter of the light-receiving aperture is small, electric noises, that is to say, thermal and electronic amplifier noises are dominant. However, when it is big, background noise becomes dominant. As a result, the total values of noises would be bigger as the diameter of the light-receiving aperture increases. Besides, shot and dark current noises would be bigger as the signal gain of the APD increases.

Thus, It's expected that we couldn't set the signal gain so big due to an increase of noises that there are proper values of the signal gain for the ToF system which can maximize detection limit while meeting the requirement of the minimum SNR of 7dB. Besides, from Fig.3.2, the diameter of light-receiving aperture should be less than 10 cm for thermal noise operation in order not to get an effect of background noise.

Next, we estimated the detection limit energy using the values of noises mentioned above with various diameters of apertures. Fig. 3.3 shows calculation results and Table. 3.2 shows the values of the parameters in this simulation.

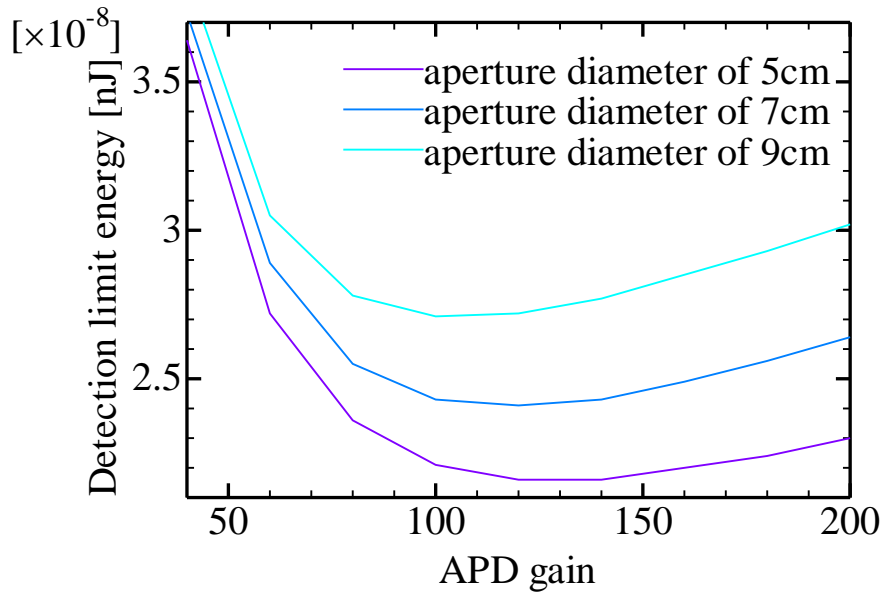


Fig. 3.3 APD gain versus detection limit energy on SNR of 7dB.

The results show the detection limit energy varies with the diameter of the light-receiving aperture. When the diameter of the light-receiving aperture is 7cm and the signal gain of the APD is 120, for example, the detection limit energy is derived to be 2.41×10^{-8} nJ with SNR of 7dB and the electrical bandwidth of 0.8GHz.

In this calculation, we assume background reflectivity ρ_B is 5 % [32] and optical bandwidth $\Delta\lambda$ is 0.25 nm [31, 32].

Table. 3.2: Values of the parameters in the detection limit calculation

Parameter	Symbol	Value
Wavelength	λ	1550 nm
Electrical bandwidth	B	0.8 GHz
Resolution		19 cm
Speed of light	c	3×10^8 m/s
Capacitance	C	1.96 pF
Resistance	R	102.8 Ω
Boltzmann constant	k	1.38×10^{-23} m ² kg s ⁻² K ⁻¹
Absolute temperature	T	300 K
Effective noise temperature	T_a	1728 K
Noise figure	NF	6.76
Material gain*	g	2000 cm ⁻¹
Waveguide loss †	α_i	15 cm ⁻¹
Optical confinement factor*	Γ	61.90%
Population inversion factor	n_{sp}	1
Input (output) coupling efficiency	$\eta_{c,in}(\eta_{c,out})$	0.3
Small signal gain*	G_0	631
Quantum efficiency	η	0.8
Elementary charge	q	1.6×10^{-19} C
Planck constant	h	6.63×10^{-34} m ² kg/s
Return signal power	P_{sig}	-45~-40 dBm
APD gain	M	10-100
Excess noise figure	F	1.62-3.08
Dark current	I_{dark}	100 nA
Solar irradiance at the Earth	S_{RR}	0.266 W / (m ² nm sr)
Background reflectivity	ρ_B	5%
Optical bandwidth	$\Delta \lambda$	0.25 nm
optical receiver efficiency	ϵ_{opt}	0.65
Incident solid angle	Ω_R	0.0123 sr
Diameter of light receiving aperture	d	5-9 cm

* Derived by simulation, † Fitted to experimental results

3.4.2 Estimate required optical pulse energy

Finally, We estimated required optical pulse energy to reach more than 200m ranging distance. In this calculation, we assumed the reflectance of the object to be -10dB, excess loss of 2dB, and internal-device loss of 3dB. As a result, total optical loss is expressed as follows [33].

$$15 + |10 \log_{10} \left(\frac{A}{2\pi L^2} \right)| \text{dB} \quad (3.38)$$

where A is the receiver aperture area, and L is the ranging distance.

Fig. 3.4 shows calculation results and Table. 3.3 shows the values of the parameters in this simulation. We assumed return optical signal energy equaled to detection limit energy. Return optical signal energy can be expressed as follows.

$$\text{Return optical signal energy} = \text{total optical pulse energy} - \{15 + |10 \log_{10} \left(\frac{A}{2\pi L^2} \right)|\} \text{dB} \quad (3.39).$$

Required optical pulse energy was estimated to be 42.0 nJ at least with the receiver aperture diameter of 7 cm and electrical bandwidth of 0.8GHz. Thus, we need to find an SOA structure whose output pulse energy is more than 0.173 nJ when the number of waveguides is 256.

Besides, when the receiver aperture diameter is 5 cm, the optical pulse energy of 72.8 nJ is required at the emitter with electrical bandwidth of 0.8GHz. In this case, we need to find an SOA structure whose output pulse is more than 0.284 nJ when the number of waveguides is 256.

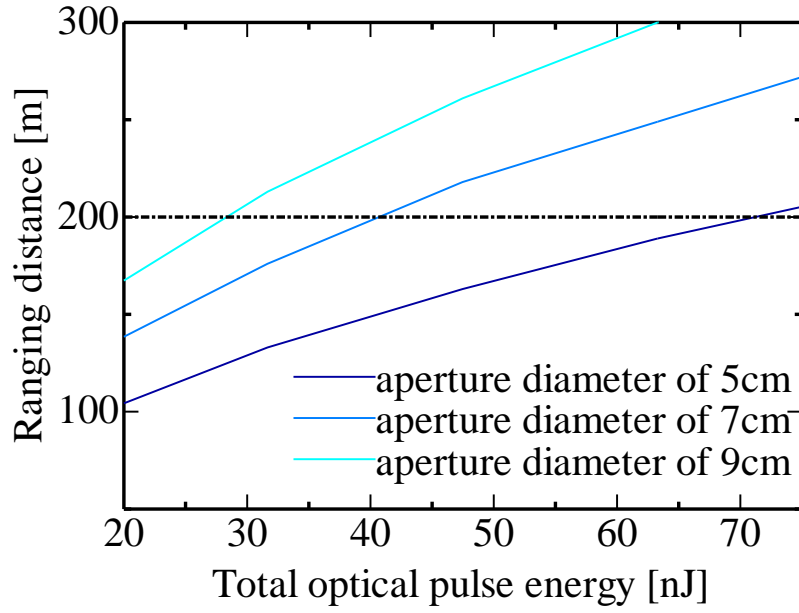


Fig. 3.4 Total optical pulse energy versus Ranging distance

Table. 3.3: Values of the parameters in the required optical pulse energy calculation

Parameter	Symbol	Value
Wavelength	λ	1550 nm
Electrical bandwidth	B	0.8 GHz
Resolution		19 cm
Speed of light	c	3×10^8 m/s
Capacitance	C	1.96 pF
Resistance	R	102.8 Ω
Boltzmann constant	k	1.38×10^{-23} m ² kg s ⁻² K ⁻¹
Absolute temperature	T	300 K
Effective noise temperature	T_a	1728 K
Noise figure	NF	6.76
Material gain*	g	2000 cm ⁻¹
Waveguide loss †	α_i	15 cm ⁻¹
Optical confinement factor*	Γ	61.90%
Population inversion factor	n_{sp}	1
Input (output) coupling efficiency	$\eta_{c,in}(\eta_{c,out})$	0.3
Small signal gain*	G_0	631
Quantum efficiency	η	0.8
Elementary charge	q	1.6×10^{-19} C
Planck constant	h	6.63×10^{-34} m ² kg/s
Return signal power	P_{sig}	-50~-40 dBm
APD gain	M	10-100
Excess noise figure	F	1.62-3.08
Dark current	I_{dark}	100 nA
Solar irradiance at the Earth	S_{IRR}	0.266 W / (m ² nm sr)
Background reflectivity	ρ_B	5%
Optical bandwidth	$\Delta \lambda$	0.25 nm
optical receiver efficiency	ϵ_{opt}	0.65
Incident solid angle	Ω_R	0.0123 sr
Diameter of light receiving aperture	d	5-9 cm
Total optical pulse energy		20-75 nJ

* Derived by simulation, † Fitted to experimental results

3.4.3 Get some material parameters from experimental results with a reference MQW

Next, we need to derive material parameters used in the simulation program explained in chapter 3.2 for finding an SOA structure whose output pulse energy is more than 0.173 nJ. We fabricated an SOA from the unoptimized epitaxial layer with a reference MQW shown in Fig. 3.5. The epitaxial layer structure used to derive material parameters has a multiple quantum well (MQW) active layer which consists of six InGaAsP 0.4% compressive strain wells with 8 nm width and seven InGaAsP 0.3% tensile strain barrier layers with 8 nm width operating at an eye-safe 1550nm wavelength.

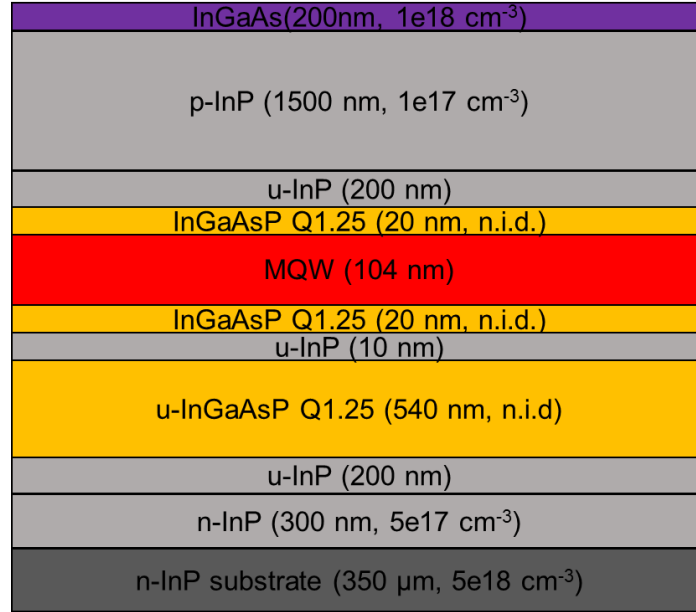


Fig. 3.5 Epitaxial layer structure used to derive material parameters

Tab. 3.4 Parameters used in the model (18 °C)

Parameter	Symbol	Value
Wavelength	λ	1550 nm
SOA waveguide width	w	4 μm
SOA length	L	1.4 mm
Facet reflectivity of a SOA	R	30.60%
Gain constant *	a	$1.29 \times 10^{-15} \text{ cm}^2$
Optical confinement factor *	Γ	10.3%
Carrier density at transparency †	n_0	$0.69 \times 10^{18} \text{ cm}^{-3}$
Nonradiative recombination rate †	A	$7 \times 10^8 \text{ s}^{-1}$
Bimolecular recombination rate †	B	$4 \times 10^{-10} \text{ cm}^3 \text{ s}^{-1}$
Auger recombination rate †	C	$2.52 \times 10^{-28} \text{ cm}^6 \text{ s}^{-1}$
Self-saturation coefficient †	ε_{11}	$1.68 \times 10^{-16} \text{ cm}^3$
Cross-saturation coefficient †	ε_{12}	$3.47 \times 10^{-16} \text{ cm}^3$
Waveguide loss †	α_i	10 cm^{-1}
Fiber coupling loss		7 dB

* Derived by simulation, † Fitted to experimental results

Fig.3.6 shows the fabrication process flow of an SOA. The details about each process are written in chapter 4. Fig. 3.7 shows an optical micrograph and an SEM image of the fabricated device.

Fig. 3.7(a),(b) is a top and a cross-sectional view of the device respectively. The surface width on a waveguide almost matched the designed value of $2\ \mu\text{m}$, indicating that photolithography and wet etching were performed accurately. After fabricating the device, I measured its amplification characteristics with continuous wave (CW), and adjusted theoretical values into experimental results for obtaining material parameters shown in Tab. 3.4.

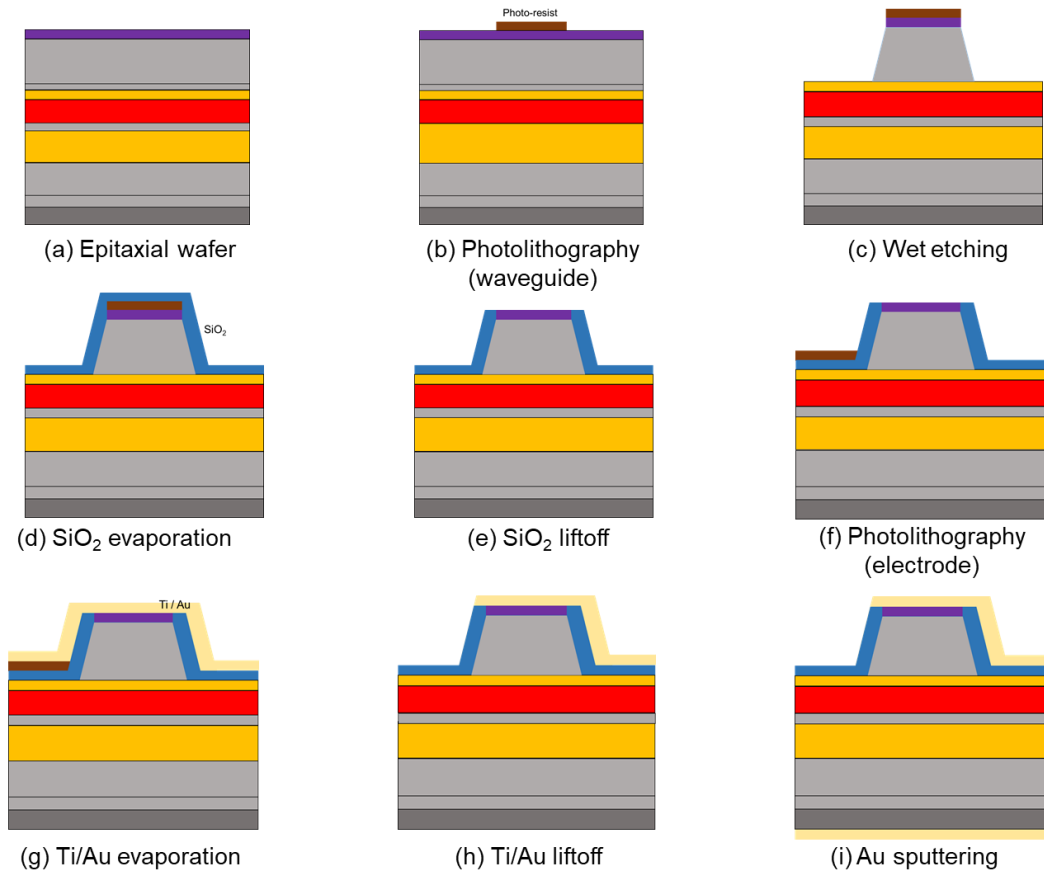


Fig. 3.6 Process flow of an SOA

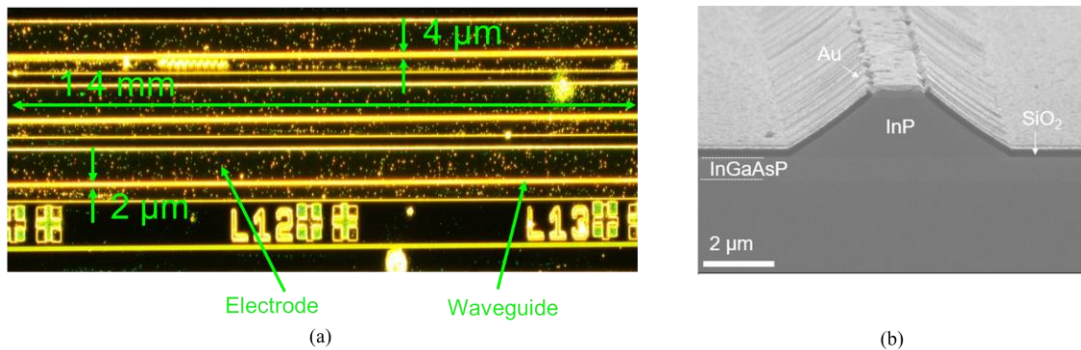


Fig. 3.7 An optical micrograph and an SEM image of the fabricated device.

(a) Top view, (b) Cross-sectional view.

The setup shown in Fig. 3.8 is used for the measurement of input versus output power characteristics on an SOA. We used an SOA with a length of 1.4 mm and a width of 4 μm in this experiment. The tunable laser diode can control the value of the input power and so can the variable optical attenuator. The polarization controllers are used to get the maximum gain in an SOA because they have the polarization-dependent gain.

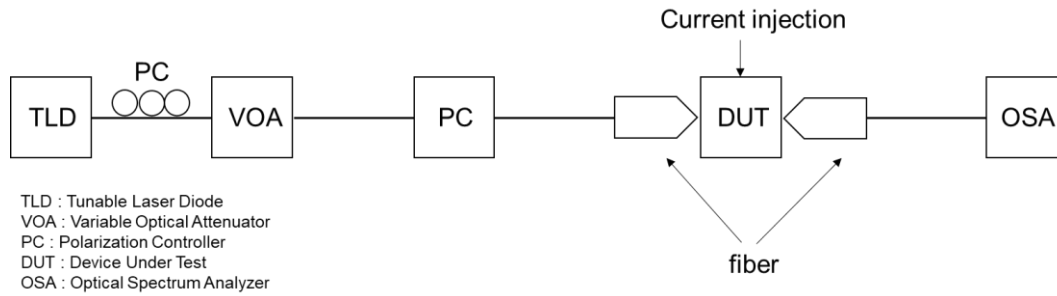


Fig. 3.8 Experimental setup for the measurement of input versus output power

Fig. 3.9 shows the results of CW input versus output power characteristics. From this figure, it can be seen that the theoretical values derived from the numerical model and the experimental values are successfully matched for each current value. The results shown in this figure are fiber-to-fiber power because we took the optical loss in the input path and output path into consideration on this numerical model. Therefore, we could get the material parameters used for simulations which are shown in Tab. 3.4.

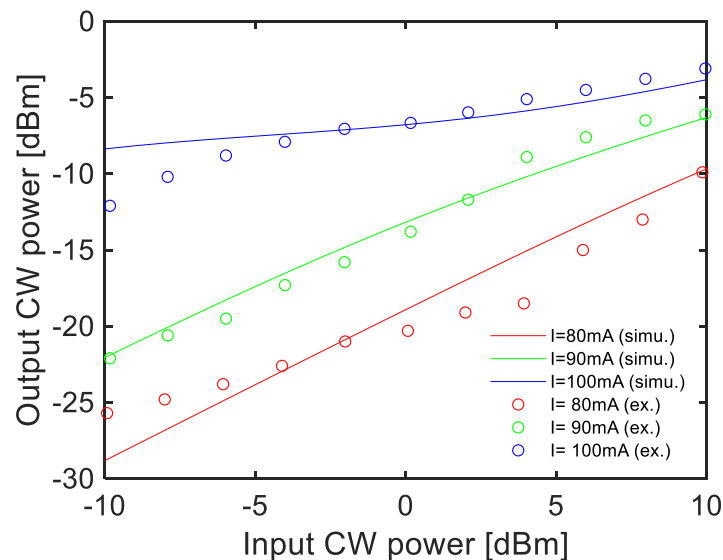


Fig. 3.9 CW input versus output power characteristics of an SOA with a length of 1.4 mm.

Solid line: theoretical values. Dash line: experimental values.

3.4.4 Optimize the epi layer structure of an SOA for an Offset QW and a Butt-joint method

We got some material parameters from CW input versus output power characteristics of an SOA made of the unoptimized epitaxial layer with a reference MQW. Thus, we can now use the numerical model for the optimization of the epitaxial layer structure for a high power SOA.

In the optimization of an SOA, we aimed at increasing the value of differential gain and optical confinement factor. There is a tradeoff between small-signal gain and saturated output power written in Eq. (2.16) and Eq. (2.17) respectively as follows [16].

$$G_{s,dB} \cdot P_{o,sat} = G_{s,dB} \left(\frac{G_s \ln 2}{G_s - 2} \right) \frac{WD}{\Gamma} \left(\frac{h\nu}{a\tau} \right) = const \quad (3.40)$$

$$G_{s,dB} \propto a\Gamma \quad (3.41).$$

It's easier to increase the value of optical confinement factor than that of differential gain, so we took the following 6 steps to increase mainly the value of optical confinement factor. For simplicity, we considered only the thickness of the core layer, well number, and length of an SOA.

When using an SOA in CW operation, it's known that reducing the optical confinement factor is better because it can increase the saturation output light intensity. However, when using an SOA in pulse operation, it may be better to increase the optical confinement factor to get high gain for a short time.

Besides, the length and width of an SOA are fixed basically to 1.4 mm and 4 μm respectively because the differential gain is dependent on not only the structure of wells but also that of an SOA.

After optimizing the epitaxial layer structure of an SOA in each case, we estimated measurable distance.

The epi layer structure used for an Offset QW method

1. decrease the thickness of the core layer from the structure shown in Fig. 3.5
2. maximize the number of wells while keeping the fundamental mode
3. change the length of an SOA
4. estimate the measurable distance using the structure optimized for an Offset QW method

The epi layer structure used for a Butt-joint method

5. maximize the number of wells while keeping the fundamental mode and strain compensation
6. estimate the measurable distance using the structure optimized for a Butt-joint method

The epi layer structure used for an Offset QW method

1. decrease the thickness of the core layer from the structure shown in Fig. 3.5

CW input versus output power characteristics was calculated for the epitaxial layer structure shown in Fig. 3.10. The difference between Fig. 3.10 (a) and (b) is the thickness of the core layer.

In this calculation, we assumed fiber coupling loss of 0 dB, facet reflectivity of 0 %, an SOA width of 4 μm , an SOA length of 1.4 mm, a temperature of 18°C, and the injection current value of 150 mA. The structure of the QW is the same as the structure shown in Fig. 3.5.

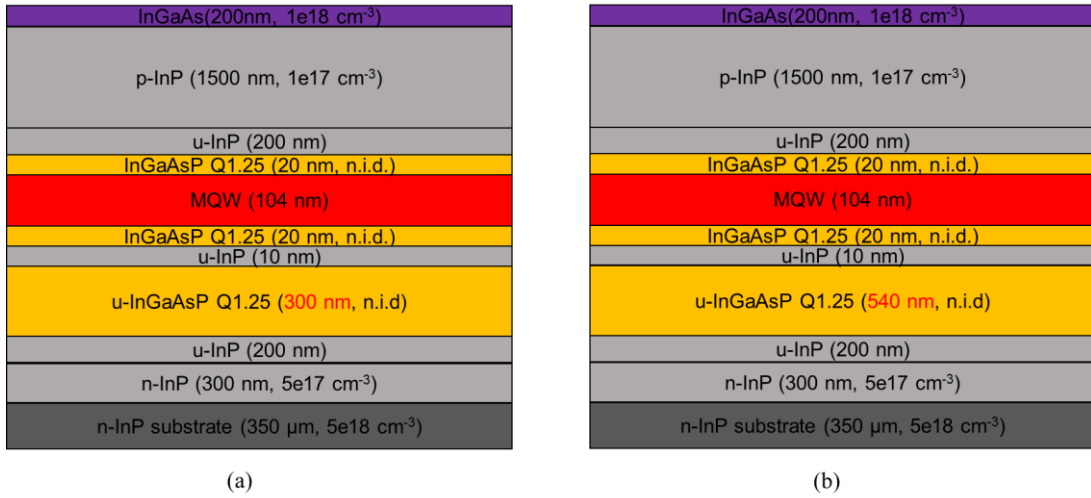


Fig. 3.10 Epitaxial layer structure used for the calculation: (a) thickness of the core layer of 300 nm. (b) thickness of the core layer of 540 nm.

Fig. 3.11 shows the results of CW input versus output power characteristics. As an input pulse power, around -5 dBm is supposed to be input to an SOA with 256 waveguides OPA assuming a gaussian pulse with a peak power of 20 dBm at the output of the input SOA (before splitting into N waveguides) (Fig. 1.8).

At - 5dBm input power, the output power of the structure having a core layer thickness of 300 nm is about 2 dB higher than that of the structure with a core layer thickness of 540 nm because of higher optical confinement factor. That's why we adopted the structure with a core layer thickness of 300 nm. The values of differential gain and optical confinement factors are written in Tab. 3.5.

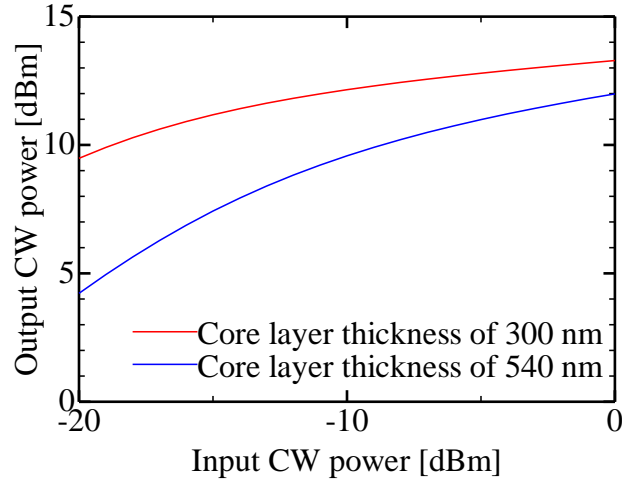


Fig. 3.11 CW input versus output power characteristics of an SOA with different core layer thicknesses

Tab. 3.5 Parameters of the values of differential gain and optical confinement factors

Core layer thickness [nm]	Differential gain a [cm^2]	Optical confinement factor Γ	$a\Gamma$ [cm^2]
300	1.29E-15	0.153	1.9737E-16
540	1.29E-15	0.103	1.3287E-16

2. maximize the number of wells while keeping the fundamental mode

CW input versus output power characteristics was calculated with the epitaxial layer structure shown in Fig. 3.12. The difference between Fig. 3.12 (a), (b), and (c) is the number of wells.

In this calculation, we assumed fiber coupling loss of 0 dB, facet reflectivity of 0 %, an SOA width of 4 μm , an SOA length of 1.4 mm, and a temperature of 18°C.

The injection current value varies with the number of wells. Each value of injection current was 150, 300, 450 mA with the well-number of 6, 12, 18 respectively. Besides, the compressive strain of wells is 0.4 % with 8nm width and the tensile strain of barrier layers is 0.3% with 8nm operating at an eye-safe 1550nm wavelength.

Speaking of strain compensation between wells and barriers, it can be written as follows.

$$d_{\text{well}}\varepsilon_{CS} = d_{\text{barrier}}\varepsilon_{TS} \quad (3.42)$$

where d_{well} , d_{barrier} are the width of well, barrier and ε_{CS} , ε_{TS} are the amount of compressive strain, tensile strain respectively. When d_{well} is 6 nm, ε_{CS} is 0.8 %, and d_{barrier} is 10 nm, required ε_{TS} is derived to be 0.48 %. A tensile strain of 0.48 % cannot be achieved from the experimental limit of crystal growth. It seems the experimental limit of a tensile strain is 0.3 % [34, 35], and when the number of quantum wells is small, the growth can be performed with no misfit transition without a perfect strain compensation [8]. It's reported that the MQW consisting of thirteen InGaAsP 1.0%

compressive strain wells with 5 nm width and fourteen InGaAsP 0.3% tensile strain barrier layers with 7 nm width was successfully fabricated.[35]. Thus, we assumed the misfit transition wouldn't occur in this calculation.

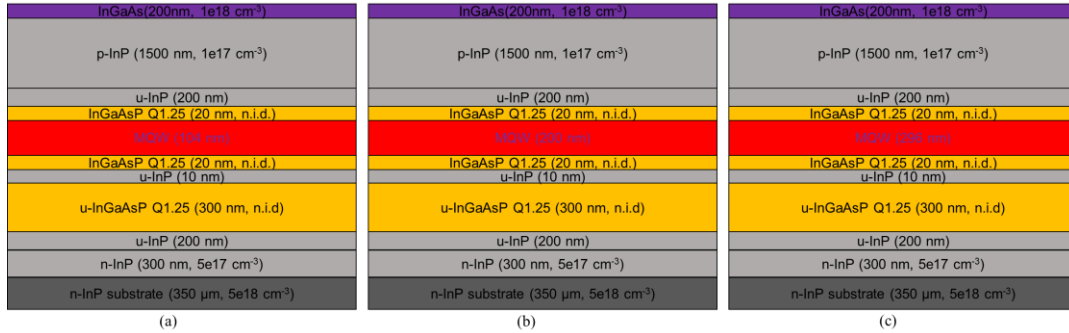


Fig. 3.12 Epitaxial layer structure used for the calculation: (a) well number of 6. (b) well number of 12. (c) well number of 18.

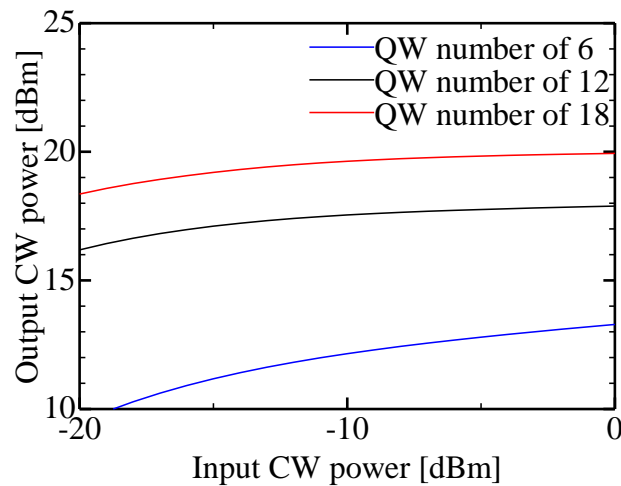


Fig. 3.13 CW input versus output power characteristics of an SOA with different well-number

Tab. 3.6 Parameters of the values of differential gain and optical confinement factors

number of wells	Differential gain a [cm^2]	Optical confinement factor Γ	$a\Gamma$ [cm^2]
6	1.29E-15	0.153	1.9737E-16
12	1.75E-15	0.327	5.7225E-16
18	1.89E-15	0.474	8.9586E-16

Fig. 3.13 shows the results of CW input versus output power characteristics with a different number of wells. The bigger the number of wells is, the higher the output power is. That's mainly because

the value of the optical confinement factor becomes big as the number of wells increases (Tab. 3.6). In addition to that, the value of differential gain also increases as the number of wells increase.

When the number of wells is over 18, the simulation result showed high order mode would occur. In order to maintain high beam quality, we adopted the well-number of 18 as the maximum number.

3.change the length of an SOA

CW input versus output power characteristics was calculated with the epitaxial layer structure shown in Fig. 3.14.

In this calculation, we assumed fiber coupling loss of 0 dB, facet reflectivity of 0 %, a temperature of 18°C, and an SOA width of 4 μm . The length of an SOA was 1.4 mm and 4.2 mm.

The injection current value varies with the length of an SOA. Each value of injection current was 450, 1350 mA with the waveguide length of 1.4, 4.2 mm respectively. Besides, the structure of the QW is the same as the structure shown in Fig. 3.12(c).

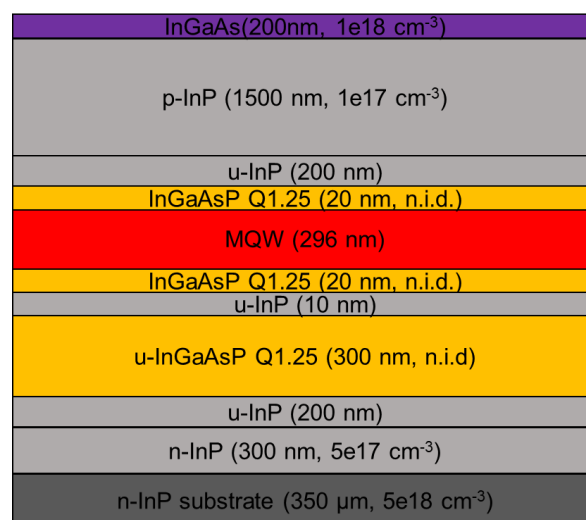


Fig. 3.14 Epitaxial layer structure used for the calculation

Fig. 3.15 shows the results of CW input versus output power characteristics with different lengths of an SOA. The difference between the structure having 1.4 and 4.2 mm is the value of differential gain shown in Tab. 3.7.

The optical output power with 4.2mm waveguide length is higher than that with 1.4mm. However, the power difference was only 1.3 dB at -5 dBm optical input power; nevertheless, the value of injection current with 4.2mm waveguide length was three times as big as that with 1.4mm. It's also important to reduce the amount of injection current. Thus, we adopted the 1.4mm waveguide length.

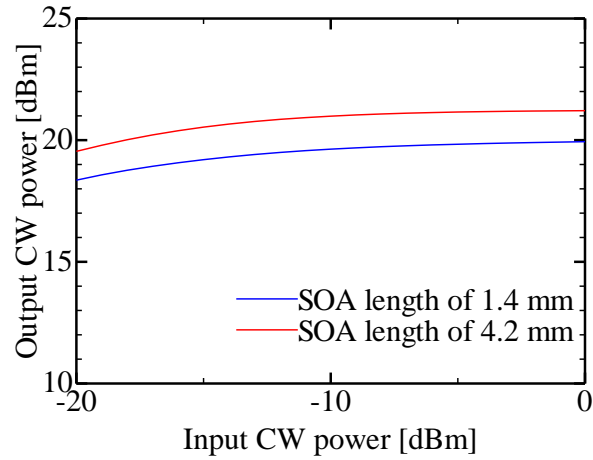


Fig. 3.15 CW input versus output power characteristics of an SOA with different SOA lengths

Tab. 3.7 Parameters of the values of differential gain and optical confinement factors

SOA length [mm]	Differential gain a [cm^2]	Optical confinement factor Γ	$a\Gamma$ [cm^2]
1.4	1.89E-15	0.474	8.9586E-16
4.2	1.96E-15	0.474	9.2904E-16

4. estimate the measurable distance using the structure optimized for an Offset QW method

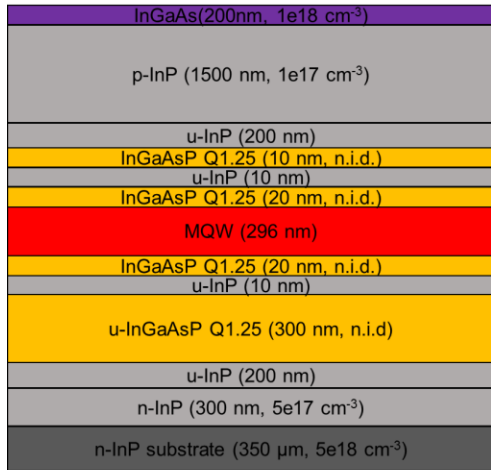
We optimized the epitaxial layer structure of an SOA for the Offset QW method in the above procedures. Next, we estimated the measurable distance for the epitaxial layer structure shown in Fig. 3.16.

Fig. 3.16(a) represents the schematic of the epitaxial layer structure and Fig. 3.16(b) is the details of that. Fig. 3.16(c) shows that high order mode doesn't occur in this layer structure.

Etching stop layers were added to the structure optimized in the above procedures. As a result, the value of optical confinement changed from 47.4% to 47.9%, and there is no change in the value of differential gain (Tab. 3.8).

Tab. 3.8 Parameters of differential gain and optical confinement factor for the optimized epitaxial layer structure

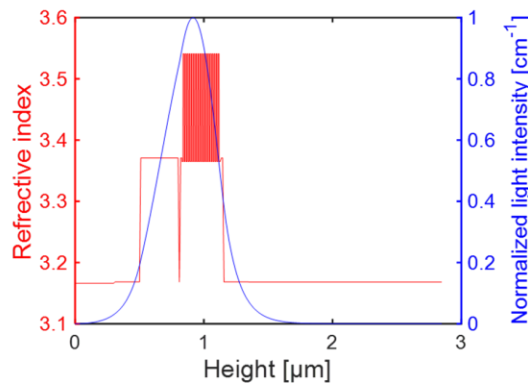
Differential gain a [cm^2]	Optical confinement factor Γ	$a\Gamma$ [cm^2]
1.89E-15	0.479	9.0531E-16



(a)

No.	Item Name	Values	Unit
1	InGaAs (Concentration)	200 (1×10^{18})	nm cm^{-3}
2	P - InP (Concentration)	1500 (1×10^{17})	nm cm^{-3}
3	U - InP	200	nm
4	U - 1.25 μm InGaAsP	10	nm
5	U - InP	10	nm
6	U - 1.25 μm InGaAsP	20	nm
7	18 \times U-InGaAsP (QW+0.4%CS)/ 19 \times U-InGaAsP (QW-0.3%TS) (λ_{PL})	8 / 8 (1540)	nm (nm)
8	U - 1.25 μm InGaAsP	20	nm
9	U - InP	10	nm
10	U - 1.25 μm InGaAsP	300	nm
11	U - InP	200	nm
12	N - InP (Concentration)	300 (5×10^{17})	nm cm^{-3}
13	InP Substrate	5×10^{18}	cm^{-3}

(b)



(c)

Fig. 3.16 Optimized epitaxial layer structure used for the Offset QW method;

(a) Schematic, (b) Profile, and (c) Refractive Index and optical mode.

We simulated the amplification of a periodic pulse train. A Gaussian pulse with a peak power of 100 mW and full width at half maximum (FWHM) of 105 ps is at the output of the input SOA (before splitting into N waveguides). Fig. 3.17 shows the output pulse waveform from each output SOA for $N = 256$ under injection current of 750 mA. The optical pulse energy within the FWHM of the output pulse is 0.187 nJ, the FWHM is 0.67 ns, and the distance resolution is 20.0 cm. The distance resolution is dependent on the value of injection current. As a result, total optical pulse energy is estimated to be 47.9 nJ.

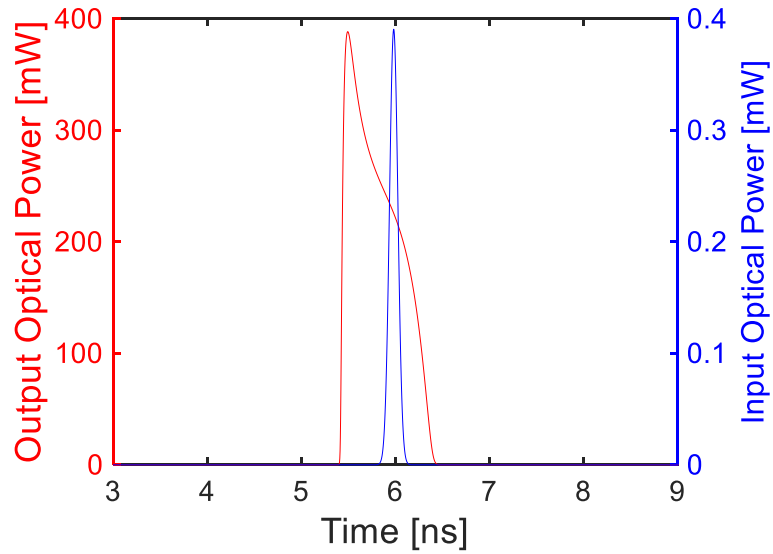


Fig. 3.17 Output pulse waveform at each output SOA with injection current of 750mA.

On the other hand, from Eq. (3.39), the measurable distance is estimated to be 210 m with the receiver aperture diameter of 7 cm and 159 m with the receiver aperture diameter of 5 cm in Fig. 3.18.

In this calculation, we assumed fiber coupling loss of 0 dB, facet reflectivity of 0 %, a temperature of 18°C, an SOA width of 4 μm , and an SOA length of 1.4 mm.

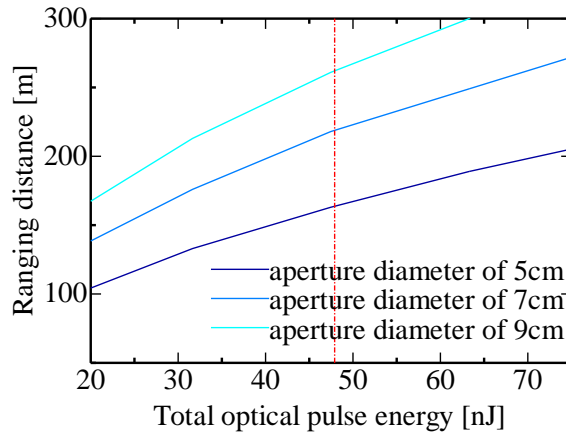


Fig. 3.18 Total optical pulse energy versus Ranging distance

The epi layer structure used for a Butt-joint method

5. maximize the number of wells while keeping the fundamental mode and strain compensation

CW input versus output power characteristics was calculated with the epitaxial layer structure shown in Fig. 3.19. The difference between Fig. 3.19 (a) and (b) is the structure of wells.

MQW in Fig. 3.19 (a) consists of thirty-three InGaAsP 0.3% compressive strain wells with 8 nm width and thirty-four InGaAsP 0.3% tensile strain barrier layers with 8 nm width. The peak of material gain is at 1.54 μm .

MQW in Fig. 3.19 (b) consists of thirty-eight InGaAsP 0.4% compressive strain wells with 6 nm width and thirty-nine InGaAsP 0.3% tensile strain barrier layers with 8 nm width. The peak of material gain is at 1.49 μm .

In both cases, the strain compensation was taken into consideration with Eq. (3.42) because the number of wells is big.

In this calculation, we assumed fiber coupling loss of 0 dB, facet reflectivity of 0 %, a temperature of 18°C, an SOA width of 4 μm , and an SOA length of 1.4 mm. The values of differential gain and optical confinement factors are written in Tab. 3.9.

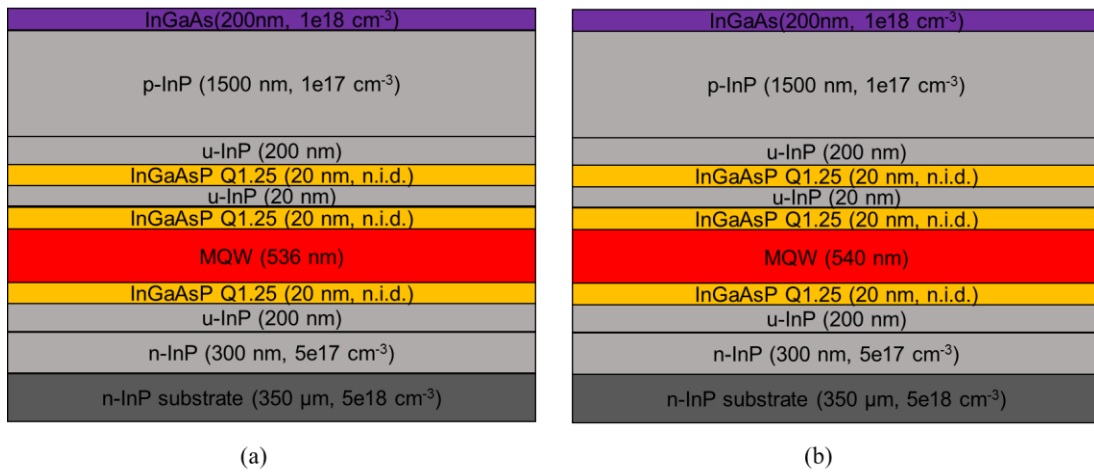


Fig. 3.19 Epitaxial layer structure used for the calculation: (a) well width of 8nm. (b) well width of 6nm..

Tab. 3.9 Parameters of the values of differential gain and optical confinement factors

Well width [nm]	Differential gain a [cm^2]	Optical confinement factor Γ	$a\Gamma$ [cm^2]
8	1.95E-15	0.816	1.5912E-15
6	1.93E-15	0.816	1.57488E-15

Fig. 3.20 shows the results of CW input versus output power characteristics with different width of wells. The injection current value was 950 mA in each case. There is no big difference in the output

power because the values of optical confinement factor and differential gain are not different greatly (Tab. 3.9).

In this research, we adopted the structure shown in Fig. 3.19 (a) because the differential gain of the structure shown in Fig. 3.19 (a) is a little bit higher than that of the structure shown in Fig. 3.19 (b).

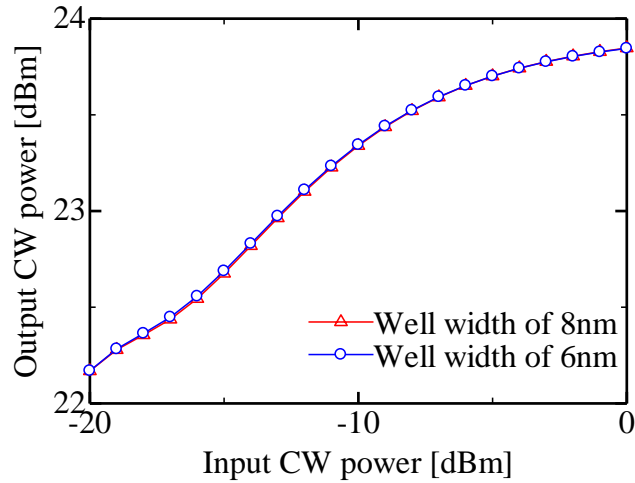


Fig. 3.20 CW input versus output power characteristics of an SOA with different well widths

Fig. 3.21(a) represents the profile of the epitaxial layer structure shown in Fig. 3.19 (a) and Fig. 3.21 (b) shows that high order mode doesn't occur in this layer structure.

No.	Item Name	Values	Unit
1	InGaAs (Concentration)	200 (1×10^{18})	nm cm^{-3}
2	P - InP (Concentration)	1500 (1×10^{17})	nm cm^{-3}
3	U - InP	200	nm
4	U - 1.25 μm InGaAsP	20	nm
5	U - InP	20	nm
6	U - 1.25 μm InGaAsP	20	nm
7	33 \times U-InGaAsP (QW +0.3%CS)/ 34 \times U-InGaAsP (QW -0.3%TS) (A_{PL})	8 / 8 (1540)	nm (nm)
8	U - 1.25 μm InGaAsP	20	nm
9	U - InP	200	nm
10	N - InP (Concentration)	300 (5×10^{17})	nm cm^{-3}
11	InP Substrate	5×10^{18}	cm^{-3}

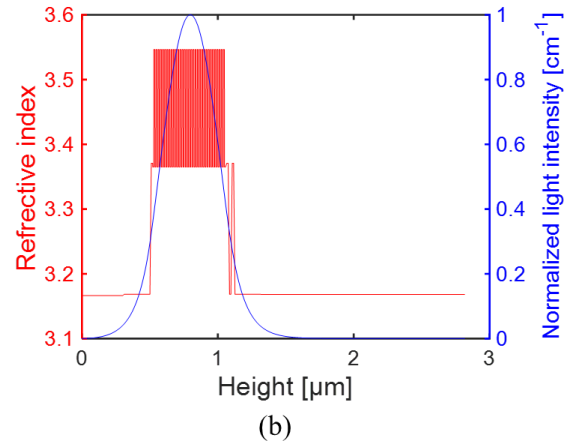


Fig. 3.21 Optimized epitaxial layer structure used for a Butt-joint method;
(a) Profile, (b) Refractive Index and optical mode.

6. estimate the measurable distance using the structure optimized for a Butt-joint method

We optimized the epitaxial layer structure of an SOA for a Butt-joint method in the above procedures. Next, we estimated the measurable distance for the epitaxial layer structure shown in Fig. 3.19 (a) and Fig. 3.21.

We simulated the amplification of a periodic pulse train. A Gaussian pulse with a peak power of 100 mW and full width at half maximum (FWHM) of 105 ps is at the output of the input SOA (before splitting into N waveguides). Fig. 3.22 shows the output pulse waveform from each output SOA for $N = 256$ under injection current of 950 mA. The optical pulse energy within the FWHM of the output pulse is 0.205 nJ, the FWHM is 0.64 ns, and the distance resolution is 19.3 cm. As a result, total optical pulse energy is estimated to be 52.4 nJ.

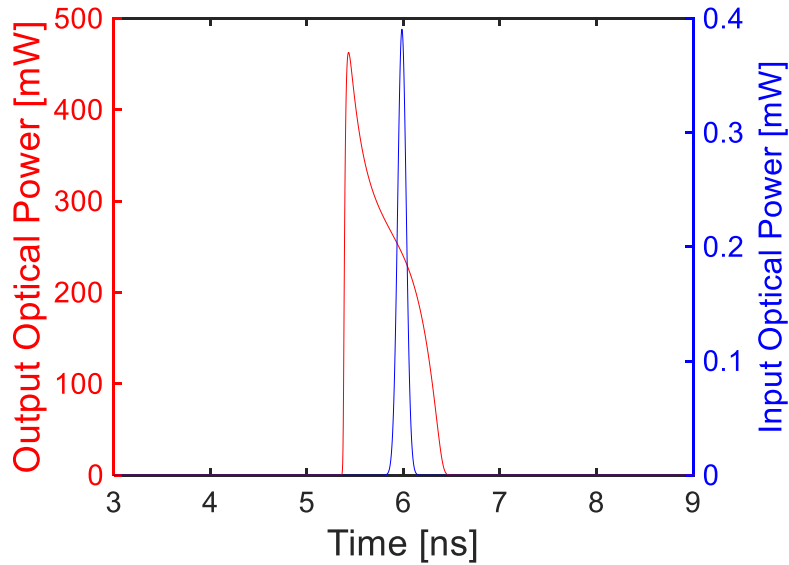


Fig. 3.22 Output pulse waveform at each output SOA with injection current of 950mA.

On the other hand, from Eq. (3.39), the measurable distance is estimated to be 225 m with the receiver aperture diameter of 7 cm and 170 m with the receiver aperture diameter of 5 cm in Fig. 3.23.

In this calculation, we assumed fiber coupling loss of 0 dB, facet reflectivity of 0 %, a temperature of 18°C, an SOA width of 4 μm , and an SOA length of 1.4 mm.

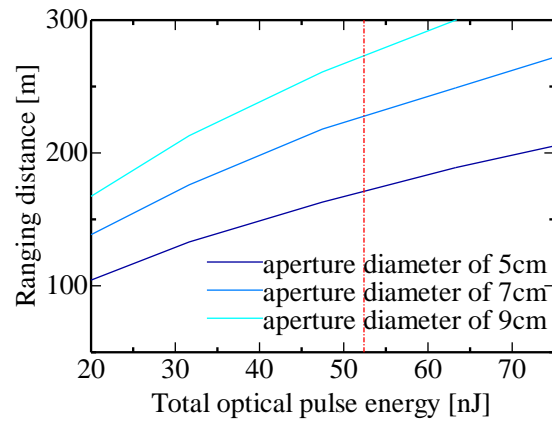


Fig. 3.23 Total optical pulse energy versus Ranging distance

Chapter 4 : Semiconductor process technology

This chapter describes the principles and characteristics of the semiconductor process used to create the SOA and OPA devices.

4.1 Deposition process

There are many techniques for forming a thin film on a semiconductor substrate, but here we outline some of the techniques used in this study.

4.1.1 spin coating

Spin coating is a technique in which a liquid material placed on a substrate is uniformly applied by centrifugal force. It's used to form thin films of organic semiconductor materials such as photoresist and polyimide dissolved in organic solvents. The film thickness is determined by the viscosity of the material and the speed of rotation. The lower the viscosity and the faster the rotation speed is, the thinner the film is formed. Therefore, even if the same material is used, the film thickness can be controlled by adjusting the speed of rotation.

Also, it should be noted that spin coating does not always provide a flat coating. The film spin-coated on a substrate with a step structure such as a waveguide is shown in Fig. 4.1. The film thickness is thinner at the thin mesa structure like a waveguide than the flat structure. The film thickness after spin coating becomes very thick near the edge of the substrate. There is not much chance to fabricate devices near the edge of the substrate, but it can be a problem in the case of photoresist. This is because the photomask and substrate are needed to be close in photolithography, so some problems such as misalignment or cracking of the substrate would occur when the thickness of the photoresist is big. In order to avoid this problem, we use a cotton swab after spin coating to remove a photoresist at the edge.

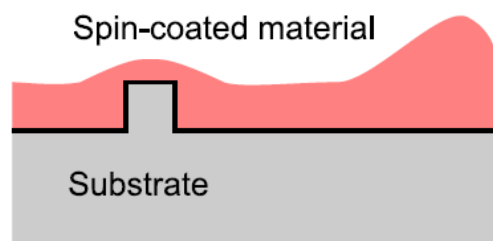


Fig. 4.1 Spin-coated material on a waveguide structure[10]

4.1.2 Vacuum deposition method

In the vacuum deposition process, the solid material is heated to evaporate, and the evaporated material adheres to the substrate. It can be classified into several methods depending on the heating method of the material. In this research, we used a beam evaporation method. The electron beam can narrow the beam diameter and the material can be heated locally so that high melting point material can be deposited. In addition to that, there is high directivity in the scattering direction of the source. When vertical deposition shown in Fig. 4.2(a) is performed with a simple waveguide structure, it's not deposited on the side of the waveguide. On the other hand, when tilted vapor deposition shown in Fig. 4.2(b) is performed, it's deposited only on one side and nothing is deposited on the shadowed part. Since directional deposition is a drawback to cover steps such as a waveguide, vapor deposition from multiple angles is used. On the other hand, the directivity of vacuum deposition works very favorably in the lift-off process described later. Also, it may be used for the self-alignment process by utilizing the characteristic of shadowing by tilted deposition[36].

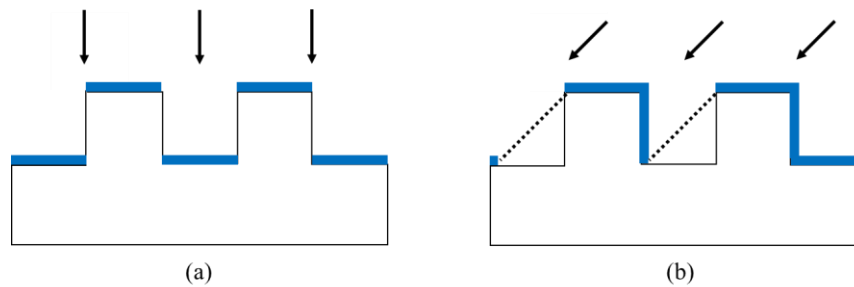


Fig. 4.2 Thin films deposited by (a) vertical evaporation and (b) tilted evaporation.

4.1.3 Sputtering

In sputtering, accelerated ions collide with the raw material (target), and scattered target adheres to the substrate. There is also the method of using an ion gun to accelerate ions, but the method of using plasma is mainstream. In order to generate plasma and prevent oxidation of deposited material, the chamber needs to be kept in a high vacuum in vacuum evaporation. On the other hand, generating a uniform plasma over a wide area is not so difficult and can cause a sputtering phenomenon from the entire surface of a disk-shaped target. Particles scattered by sputtering have more energy than vacuum deposition. That's why adhesion to the substrate and the film quality are improved. In addition, particles come from various directions on the substrate so that there is no directionality of deposition.

4.2 lithography process

The technology that forms the pattern is called lithography. In lithography, energy is applied to a part of an organic thin-film called resist applied on a semiconductor substrate to cause a reaction.

Lithography is extremely important for producing highly integrated devices. Various lithography techniques are used for the fabrication of optical semiconductor elements. In this research, the light exposure (photolithography) technology is used.

4.2.1 photolithography

Photolithography is the method to expose ultraviolet radiation to the photoresist applied on a semiconductor substrate. The patterns are transferred onto the substrate by installing a mask between the substrate and the light source when ultraviolet light is irradiated[37].

There are several methods depending on how the photomask is installed. In this study, the proximity exposure method is used because of its simplicity. In the proximity exposure method, exposure is performed with the photomask in close contact with the semiconductor substrate, and the resolution R is estimated as 2 or $3\mu\text{m}$ [37].

Table 4.1 shows the photoresist used in the fabrication process. Important factors in photoresist selection include the thickness and the type of positive and negative.

Table. 4.1 Photoresists used for fabrication

Name	Manufacturer	Posi / Nega	Typical thickness	Note
S1805	Shipley	Positive	600 nm	
TSMR8900	Tokyo Ohka Kogyo	Positive	1.3 μm	
AZ5214E	Microchemicals	Negative	1.5 μm	Posi / Nega available
AZ5200NJ	Microchemicals	Negative	3 μm	Posi / Nega available

When negative/positive is reversed, the pattern formed is inverted. Besides, that change can also be caused by inverting the negative/positive of the mask pattern. There are two points to consider when deciding negative/positive.

1. Generally, positive resists have better pattern accuracy. Therefore, a positive resist is used for a detailed pattern such as a waveguide.
2. When performing photolithography using negative or positive resist with the same photomask pattern, the combined pattern has the shape shown in Fig. 4.3.

Regarding the thickness, a thin resist can generally form a high-definition pattern. It must be thick enough for processes such as a dry etching in which a resist can be removed. AZ5214E and AZ5200NJ listed in Tab. 4.1 can be used as both negative and positive resists. Specifically, it works as a positive resist at the stage of exposure of the pattern. The negative and positive are reversed by

performing the whole surface exposure and baking called post reversal bake. In this study, these two types of resists were always used as negative resists.

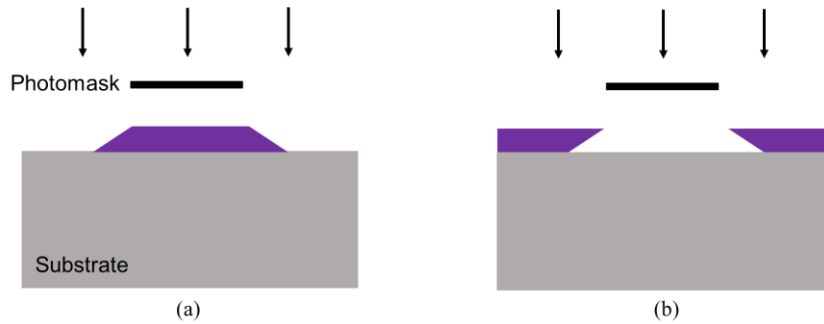


Fig. 4.3 Patterns after photolithography with (a) positive resist and (b) negative resist.

4.2.2 Lift off

The lift-off process forms thin film patterns of various inorganic materials by lithography and vacuum deposition, which is not widely used in industry but often used at the research level. As an example, Fig. 4.4 shows the flow of the lift-off for gold. Firstly, patterning by lithography and vacuum deposition is performed. Then, the thin film deposited on the resist is simultaneously removed by removing the resist. As a result, the gold pattern is formed only on the part without resist.

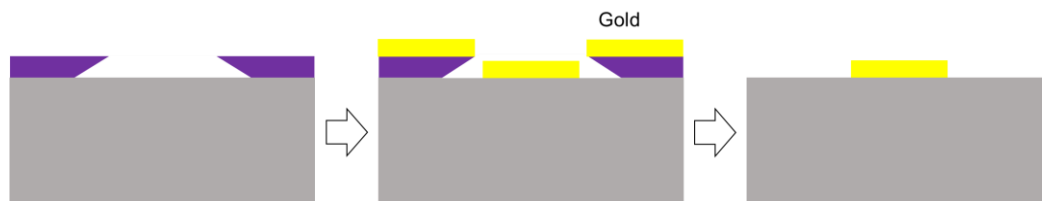


Fig. 4.4 Procedure of gold patterning through the lift-off

An organic solvent such as acetone is used to remove the resist. The important point in the lift-off process is that the part supposed to be removed and left are separated after deposition. If the thin film completely covers the resist, the organic solvent cannot penetrate. In addition to making it difficult to remove the resist, even if it can, the connected thin film will be physically torn and a good pattern cannot be obtained. It's desirable that the resist film thickness should be as thick as possible to simplify the lift-off.

4.3 Etching

The etching is the process of scraping material on the substrate as opposed to film formation. A chemical reaction is mainly used in etching. Patterns formed by photolithography are used mainly as the mask to scrap the part having no patterns.

There are two main types of etching methods. Wet etching is performed by immersing a sample in a chemical solution. On the other hand, dry etching is performed in a plasma gas. In this research, wet etching is used. The following outlines the wet etching technology.

Wet etching

Wet etching is performed by immersing the substrate in a solution called an etchant. The material on the substrate is scraped off purely by a chemical reaction because the process is in solution. The ratio between the thickness of the mask and the object is called the selection ratio. A selection ratio close to infinity can be obtained by selecting an etchant and a mask properly.

On the other hand, since ions and molecules in the solution move isotropically, the etching proceeds even to the bottom of the mask. That's why phenomenon such as undercutting or etching progressing along the crystal plane occurs.

For example, a stripe pattern is etched using HCl and H₃PO₄ on an InP substrate with the (001) plane as the substrate surface. As shown in Fig. 4.5, the stripes in the [110] direction have almost vertical or tilted over 90 degrees, but in the $[\bar{1}10]$ direction, they have an inclination of 35 degrees[38]. Such anisotropy exists. Therefore, it's necessary to consider the crystal orientation of the substrate in the manufacturing process including wet etching.

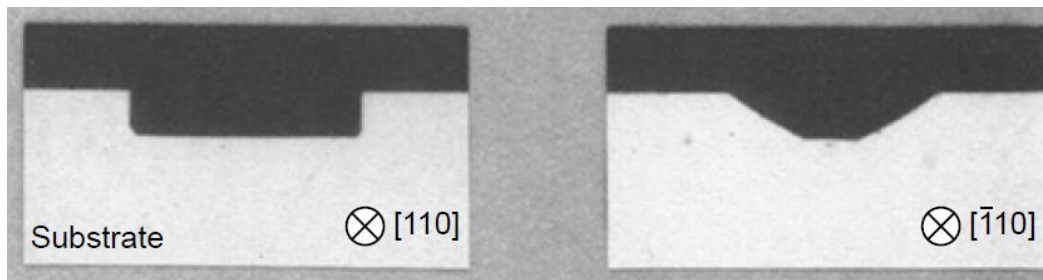


Fig. 4.5 Cross-sectional image of InP with stripes along [110] and $[\bar{1}10]$ direction etched by HCl and H₃PO₄ [38].

Table 4.2 shows material etched by wet etching and etchants used in this study. InP is etched by a mixture of hydrochloric acid and phosphoric acid, but does not react with sulfuric acid or hydrogen peroxide. Conversely, InGaAs and InGaAsP are etched with a mixture of sulfuric acid and hydrogen peroxide, but not etched with phosphoric acid. Therefore, for example, An InGaAsP layer of about 10 nm can be used as an etch stop layer when etching the InP layer.

Table. 4.2 Etching material and etchants used for wet etching

Material to be etched	Etchant	Temperature
InP	HCl:H ₃ PO ₄ = 1:3	R. T.
InGaAs, InGaAsP	H ₂ SO ₄ :H ₂ O ₂ :H ₂ O = 1:1:5	5°C

4.4 Crystal growth technology

Crystal growth technology for growing semiconductor crystals on a substrate is extremely important in fabricating high-quality optical semiconductor devices. Although several techniques for crystal growth have been put into practical use, we outline metal-organic vapor phased epitaxy (MOVPE) used in this study.

Fig. 4.6 shows the schematic of the MOVPE device. Organometallic raw material gas is mixed with a carrier gas (hydrogen) and then carried into the reactor in which the installed semiconductor substrate exists to perform epitaxial growth. Controlling the partial pressure ratio of each source gas in all gases can control the atomic composition ratio in the crystal with a high degree of freedom. Important parameters for crystal growth are the growth temperature and the gas phase composition of each source gas. The solid phase composition in the crystal can be varied in various ways by precisely controlling the gas phase composition. The lattice constant of the growing crystal generally should match that of the substrate during the growth. If the difference is large, it will cause many defects.

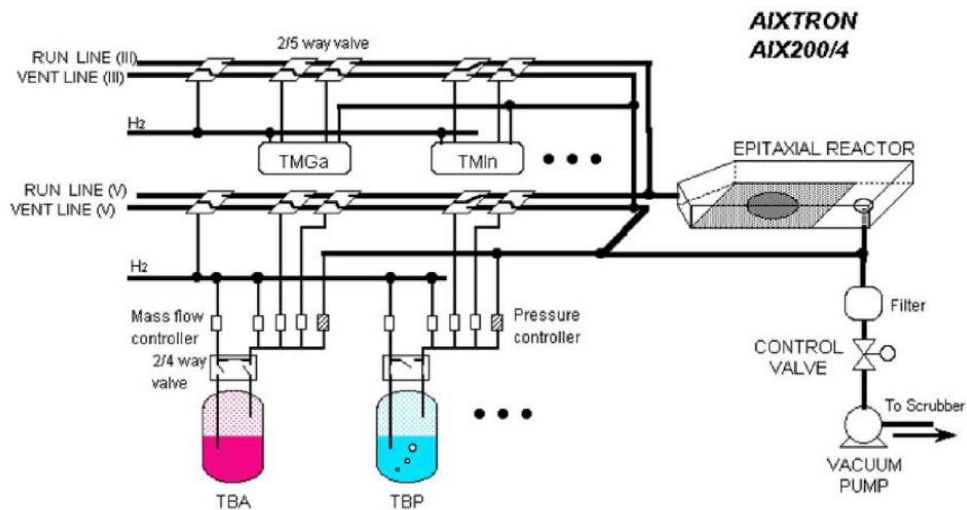


Fig. 4.6 Schematic of the MOVPE device[37].

Chapter : 5 Fabrication and measurement

This chapter describes the fabrication and measurement results.

5.1 Crystal growth for the sample with high compressive strain wells

We performed the crystal growth to fabricate the epitaxial layer structure shown in Fig. 5.1. MQW in Fig. 5.1 consists of five InGaAsP 0.8% compressive strain wells with 6 nm width and six InGaAsP 0.5% tensile strain barrier layers with 10 nm width. The peak of material gain is at 1.54 μm .

The reason why the epitaxial layer structure is different from the structure calculated in chapter 3 is we fabricated the structure shown in Fig. 5.1 before precise optimization described in chapter 3.

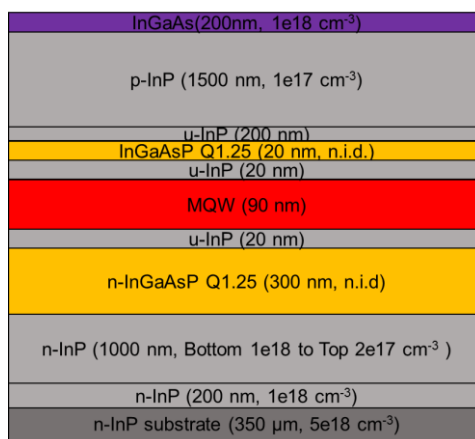
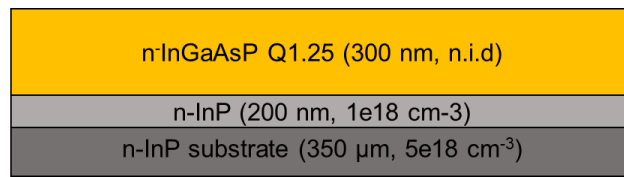


Fig. 5.1 Epitaxial layer structure supposed to be fabricated

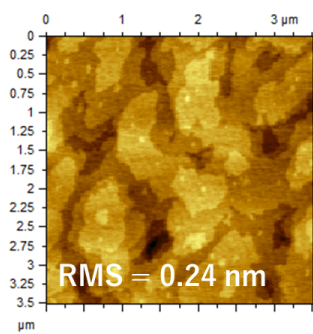
Firstly, we performed the crystal growth to find conditions for the InGaAsP core layer. The grown substrate structure is shown in Fig. 5.2(a).

Fig. 5.2(b) is the resulting image of an Atomic Force Microscope (AFM) measurement. AFM is a type of Scanning Probe Microscope (SPM), which uses the atomic force between the sample and stylus to obtain nano level irregularity information. Root Mean Square (RMS) represents the surface roughness of the InGaAsP core layer. 0.24 nm is two-fifth as small as InGaAsP lattice constant of 0.5869 nm so we concluded that the crystal quality was not so bad. However, it should be smaller if possible.

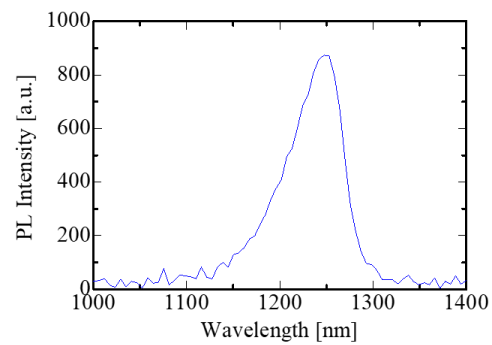
Fig. 5.2(c) is the result of Photo Luminescence (PL) measurement. PL refers to the process by which a substance absorbs and re-emits light. When the light having energy larger than the bandgap of the semiconductor is irradiated, electrons in the semiconductor are excited, and electrons and holes are formed. Then, more electrons and holes are formed than in thermal equilibrium. Afterward, excited electron energy is emitted as light. As a result, the wavelength of the bandgap can be determined. It's estimated that the bandgap wavelength of this InGaAsP is 1.25 μm from Fig. 5.2(c).



(a)



(b)



(c)

Fig. 5.2 Growth for the InGaAsP core layer;

- (a) The grown substrate structure, (b) The image of AFM measurement,
(c) The result of PL measurement.

Next, we performed the crystal growth to find conditions for the InGaAsP MQW. The grown substrate structure is shown in Fig. 5.3(a). Fig. 5.3(b) is the result of the PL measurement. The power of excitation light is 337mW in each case of S1 and S2.

MQW in S1 consists of five InGaAsP 0.8% compressive strain wells with 6.3 nm width and six InGaAsP 0.08% compressive strain barrier layers with 8.5 nm width.

MQW in S2 consists of five InGaAsP 0.8% compressive strain wells with 6.8 nm width and six InGaAsP 0.08% compressive strain barrier layers with 6 nm width.

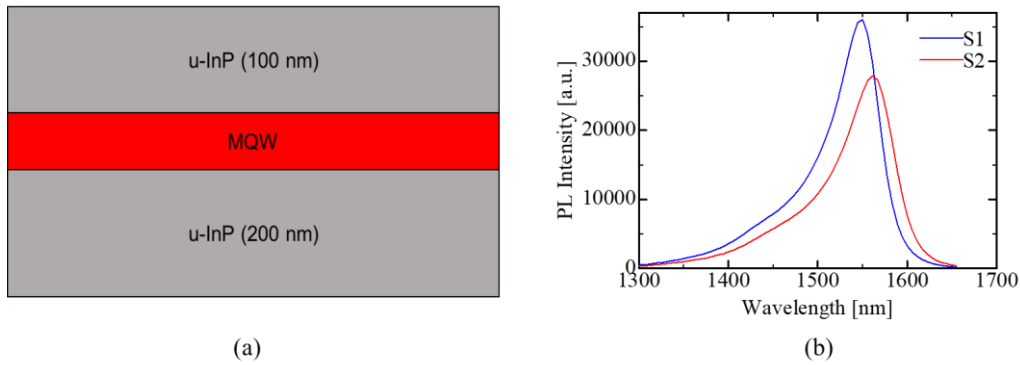


Fig. 5.3 Growth for InGaAsP MQW;

(a) The grown substrate structure, (b) The result of the PL measurement.

This result shows that when the number of wells is small, it doesn't reach the critical film thickness with no strain compensation. However, if possible, it should take strain compensation for high-quality crystal even if the growth can be performed with no strain compensation.

It can be regarded as non-strain, although the barrier layer has a 0.08% compressive strain. That's why the PL intensity of the S1 structure is higher than that of S2 one because the width of the barrier layer in S1 is thicker than that in S2. It's known from Eq. (3.42) that the thicker the width of the barrier layer is, the smaller the required tensile strain is.

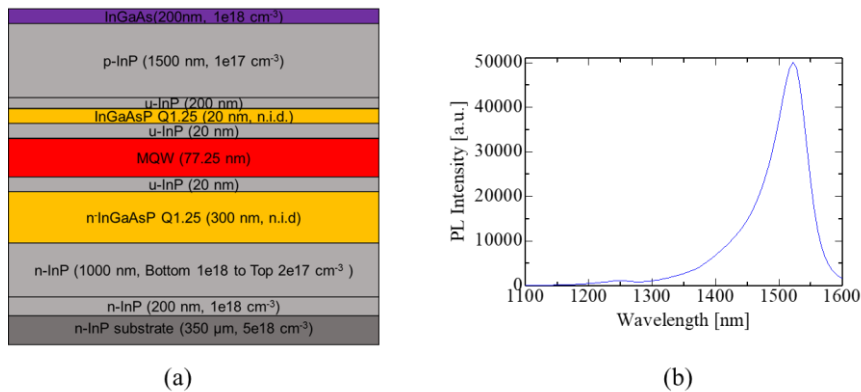


Fig. 5.4 Growth for the InGaAsP MQW;

(a) The grown substrate structure, (b) The result of the PL measurement.

Finally, we performed the crystal growth to fabricate the epitaxial layer structure shown in Fig. 5.4(a) using the conditions we found. MQW in Fig. 5.4(a) consists of five InGaAsP 0.8% compressive strain wells with a width of 5.25 nm and six InGaAsP 0.08% compressive strain barrier layers with a width of 8.5 nm. The peak of material gain is at 1.52 μm shown in Fig. 5.4(b). The power of excitation light is 337mW.

Both the width of wells and barriers were shifted by about 1 nm due to the difference of the layers under the MQW in the case of Fig. 5.3(a) and Fig. 5.4(a).

5.2 Fabrication of the laser

Next, we fabricated a laser using the grown substrate shown in Fig. 5.4(a) to estimate the net gain described in Appendix A. The fabrication process flow of a laser is the same as that of an SOA described in Fig. 3.6.

Fig. 5.5(a) is a top view of the device, Fig. 5.5(b) is a cross-sectional view of the device and Fig. 5.5(c) is a cross-sectional enlarged view of the device. The surface width on a waveguide almost matched the designed value of 4 μm from Fig. 5.5(b), indicating that photolithography and wet etching were performed accurately. Besides, SiO_2 and Au were deposited properly from Fig. 5.5(b) and (c). The fabricated substrate was fixed on a copper plate by heating at 120 degrees for one hour using silver paste.

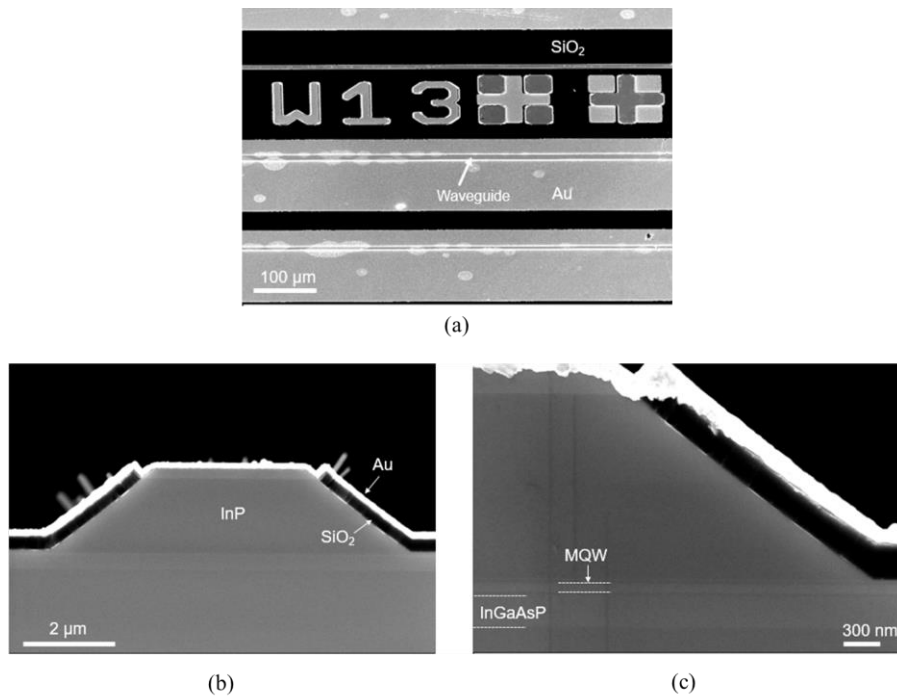


Fig. 5.5 SEM image of the fabricated device.

(a) Top view, (b) Cross-sectional view, (c) Enlarged cross-sectional view.

5.3 Measurement results of the laser

5.3.1 Current-Voltage characteristics

First, the current-voltage characteristics of the laser were evaluated. Fig. 5.6 shows the measurement result with a waveguide length of 4 mm and a width of 3 μm , 4 μm , and 8 μm . The threshold voltage is generally consistent at around 0.5 V.

Given a resistive material, the relationship between the resistance R and the cross-sectional area A is expressed as $R = \rho l/A$, where ρ is the electric resistivity and l is the length in the current flow direction. Thus, It's known the value of resistance is reverse proportional to the cross-sectional area.

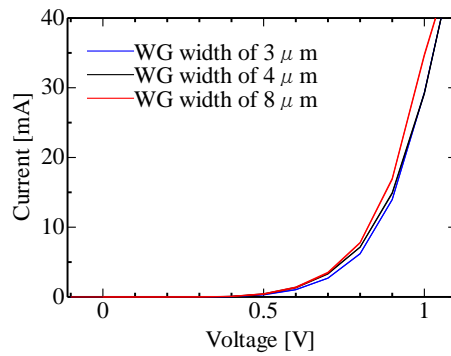


Fig. 5.6 Current-Voltage characteristics of a laser

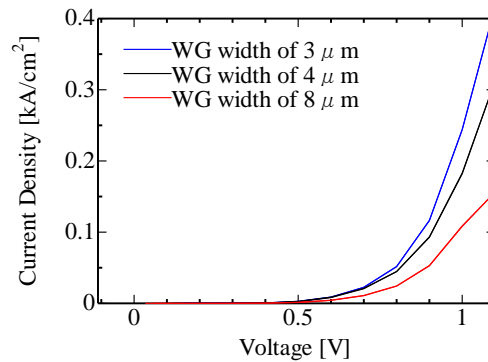


Fig. 5.7 Current density-Voltage characteristics of a laser

To make a fair comparison for the value of overall resistance, we evaluated current density-voltage characteristics shown in Fig. 5.7. Assuming the same length in the current flow direction, the wider waveguide gives higher overall resistance in comparison to shorter ones. This might be because the number of defects on the device surface could be bigger when the waveguide width is larger.

5.3.2 Optical characteristics

Next, the optical characteristics of the laser were evaluated. We measured ASE (Amplified Spontaneous Emission) characteristics with current injection using the Optical Spectrum Analyzer (OSA) shown in Fig. 5.8.

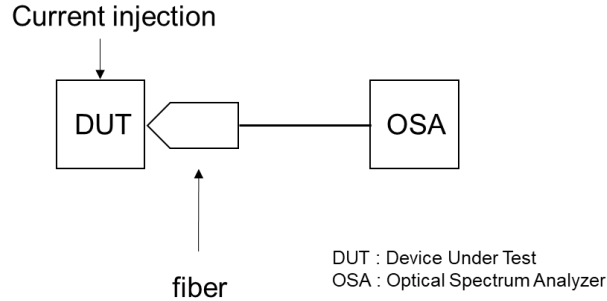


Fig. 5.8 Experimental setup for the measurement of ASE characteristics

Fig. 5.9 shows the results of ASE characteristics. The length of the lasers is 4 mm in each case. The width of the laser in Fig. 5.9(a) is 3 μm and that in Fig. 5.9(b) is 4 μm .

From these figures, it can be seen that lasing didn't occur in each case even when the value of the current injection increased. we suspect the reason could be the low gain due to no strain compensation in the crystal growth described in chapter 5.1. Thus, we need to reconsider the structure with strain compensation.

Besides, the gain threshold is expressed as follows.

$$g_{th} = \alpha + \frac{1}{2L} \ln \frac{1}{R^2} \quad (5.1)$$

where α is an internal loss, L is the laser length, and R is facet reflectivity of the laser. If we assume α of 10 cm^{-1} , L of 4 mm, and R of 30.6 %, g_{th} is estimated to be 13 cm^{-1} .

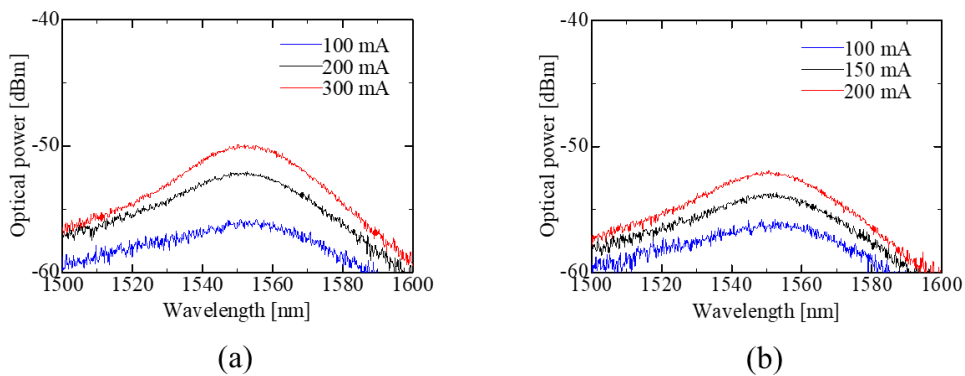


Fig. 5.9 ASE characteristics for different current.

(a) the laser width of 3 μm , (b) the laser width of 4 μm .

5.4 Crystal growth for the sample with high optical confinement factor

We performed the crystal growth to fabricate the epitaxial layer structure with strain compensation shown in Fig. 5.10. MQW in Fig. 5.10 consists of thirty-three InGaAsP 0.3% compressive strain wells with 8 nm width and thirty-four InGaAsP 0.3% tensile strain barrier layers with 8 nm width. The peak of material gain is at 1.54 μm . Besides, the bandgap-wavelength of the well layer is 1.6 μm and that of the barrier layer is 1.25 μm .

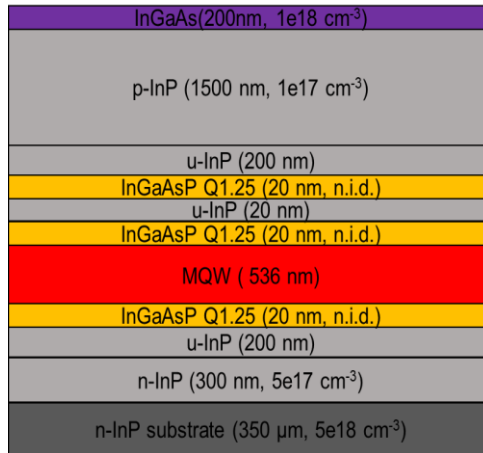


Fig. 5.10 Epitaxial layer structure supposed to be fabricated

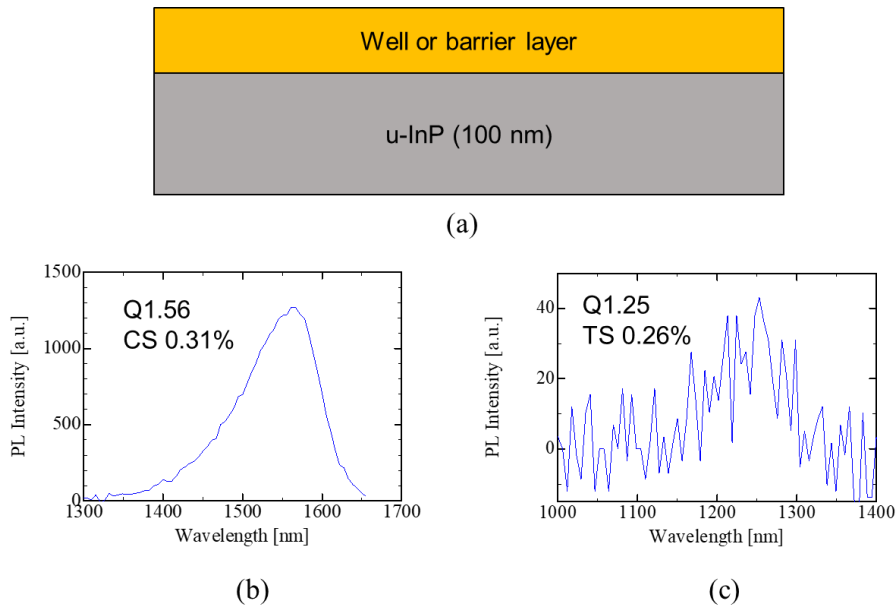


Fig. 5.11 Growth for gaining conditions of the well and barrier layer;

- (a) The grown substrate structure, (b) The result of PL measurement for the well layer,
- (c) The result of PL measurement for the barrier layer.

Firstly, we performed the crystal growth to find conditions for the well and barrier layers. The grown substrate structure is shown in Fig. 5.11(a).

Fig. 5.11(b), (c) is the result of PL measurement. It's derived that the bandgap-wavelength of the well layer is $1.56\ \mu\text{m}$ with compressive strain 0.31% and that of the barrier layer is $1.25\ \mu\text{m}$ with tensile strain 0.26%.

Next, we performed the crystal growth to find conditions for the InGaAsP MQW. The grown substrate structure is shown in Fig. 5.12(a). MQW consists of thirty InGaAsP 0.31% compressive strain wells with the bandgap-wavelength of $1.56\ \mu\text{m}$ and thirty-one InGaAsP 0.26% tensile strain barrier layers with the bandgap-wavelength of $1.25\ \mu\text{m}$.

Fig. 5.12(b) shows the result of the X-ray diffraction (XRD) measurement. From this result, the width of the well and barrier layer were derived to be 9.2 nm and 9.14 nm respectively. Besides, the peak of the material gain was derived to be $1.52\ \mu\text{m}$ from Fig. 5.12(c).

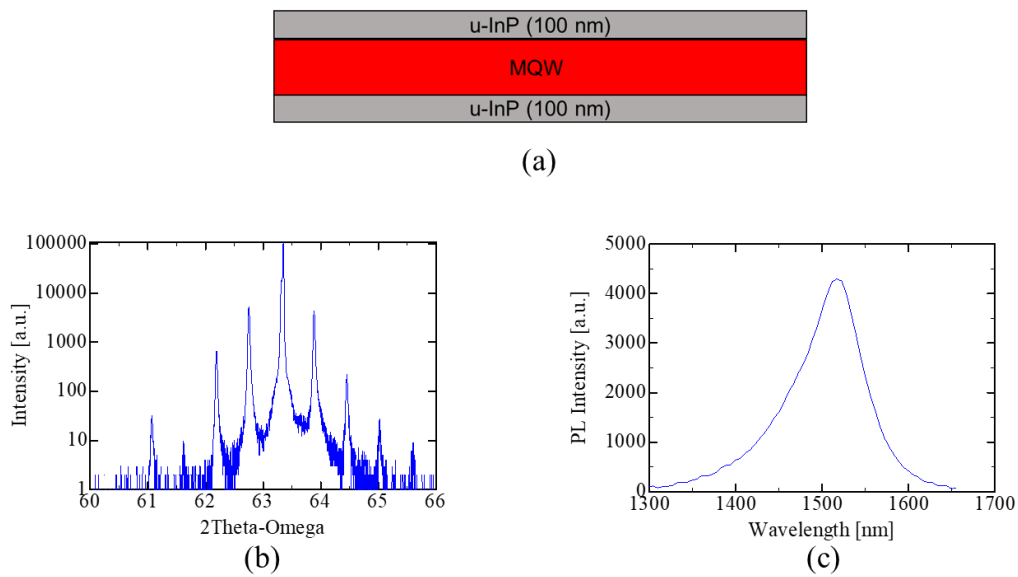


Fig. 5.12 Growth for gaining condition of the MQW;

- (a) The grown substrate structure, (b) The result of XRD measurement,
(c) The result of PL measurement.

Chapter : 6 Conclusion

6.1 Summary of this research

We worked on the research about the InP-based OPAs with integrated SOAs, operating at an eye-safe 1550-nm wavelength to achieve high output pulse energy necessary for ToF LiDAR applications.

We first calculated the detection limit energy of the ToF system at the receiver and required optical pulse energy at the emitter. The detection limit energy at the receiver in the ToF system was estimated to be 2.41×10^{-8} nJ with SNR of 7dB and an electrical bandwidth of 0.8 GHz. On the other hand, the optical pulse energy of 44.3 nJ seemed to be necessary to reach more than 200m ranging distance when the diameter of light-receiving aperture is 7 cm. That is to say, an SOA having output pulse energy of more than 0.173 nJ is indispensable when the number of OPAs waveguide is 256.

We secondly optimized an epitaxial layer structure of an SOA having more than 0.173 nJ optical pulse energy with a numerical model based on the rate equation and then estimated the measurable distance. Before optimization of an SOA, a ridge waveguide SOA was fabricated and we measured input/output characteristics to get some material parameters for the numerical model. The result showed good agreement was obtained at a respective current between experimental and theoretical values.

In the optimization of an SOA, we aimed at increasing the optical confinement factor mainly. After the optimization finished, we simulated the amplification of a periodic pulse train. A Gaussian pulse with a peak power of 100 mA and FMHW of 105ps was assumed at the output of input SOA shown in Fig. 1.8 (before splitting into N waveguides).

The results showed the optical pulse energy within the FWHM of the output pulse was 0.205 nJ, the FWHM was 0.64 ns, and the distance resolution was 19.3 cm. Thus, total optical pulse energy was estimated to be 52.4 nJ. As a result, the measurable distance was estimated to be 225 m with the receiver aperture diameter of 7 cm and 170 m with the receiver aperture diameter of 5 cm.

Finally, We performed the crystal growth to gain conditions for fabricating an epitaxial layer structure we designed.

6.2 Future issue and prospect

The major issue discovered in this study is the crystal growth. It was so hard to fabricate high compressive strain wells with high quality by hand. Quality of the crystal is important for an SOA to get high gain so that it might be better to consider fabricating less than 0.3% compressive strain or non-strain wells for the high quality of the crystal. That's because the experimental limit of a tensile strain is known to be 0.3 %.

As a prospect, it seems better to consider InP-based OPAs with integrated SOAs, operating at around 1480-nm wavelength. That's because the effect of solar irradiance at the Earth can be suppressed greatly when using around 1480-nm wavelength. Fig. 6.1 shows the relationship between wavelength and the spectral irradiance of the sun. Thus, the effect of background noise can be reduced greatly. As a result, SNR would be improved in comparison to that of OPAs operating at 1550-nm so that the diameter of the light-receiving aperture might be able to be smaller.

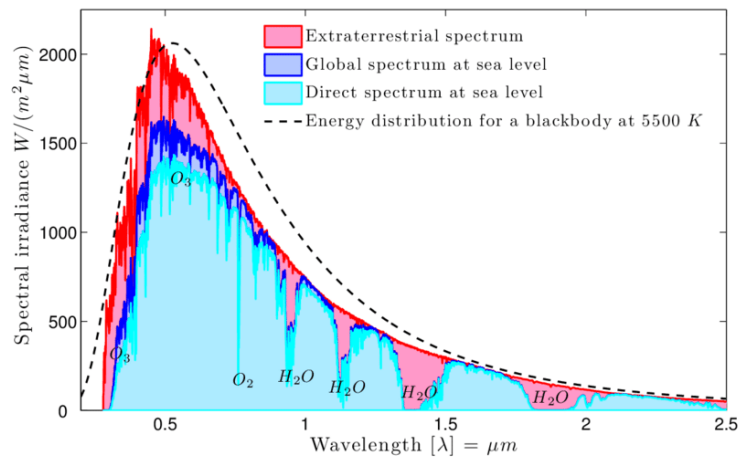


Fig. 6.1 The spectral irradiance of the sun [39].

Appendix A : How to estimate the net Gain from Lasing

The net gain G_i is expressed as follows [40].

$$G_i = \frac{1}{\Gamma L} \ln \left(\frac{\gamma_i^{0.5} + 1}{\gamma_i^{0.5} - 1} \right) + \frac{1}{\Gamma L} \ln R \quad (\text{A-1})$$

$$\gamma_i = \frac{P_i + P_{i+1}}{2V_i} \quad (\text{A-2})$$

where γ_i is the depth of modulation, $\frac{1}{2}(P_i + P_{i+1})$ is the average values of two consecutive peaks, V_i is the intermediate valley of two consecutive peaks, L is the length of the laser, Γ is optical confinement factor in the active layers, and R is the facet reflectivity of the laser.

For example, Fig. A.1 is one example of laser lasing. The net gain G_i is estimated to be 59.2 cm^{-1} from Fig. A.1(b) with two consecutive peak values of $28.8 \mu\text{W}$ at the wavelength of 1440.9 nm and $0.722 \mu\text{W}$ at the wavelength of 1442.1 nm , the intermediate valley value of $0.0161 \mu\text{W}$ at the wavelength of 1441.6 nm , the laser length of 1.8 mm , and optical confinement factor of 10.5% .

On the other hand, the gain threshold is derived to be 16.6 cm^{-1} from Eq. (5.1), when we assume α of 10 cm^{-1} , and R of 30.6% .

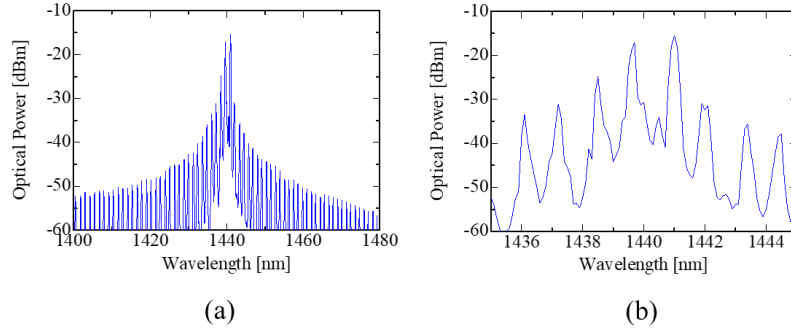


Fig. A.1 The schematic of lasing characteristics.

(a) with wide range of the wavelength, (b) with narrow range of the wavelength.

Bibliography

- [1] “How Google's Self-Driving Car Works,” *IEEE Spectrum*, <http://spectrum.ieee.org/automaton/robotics/artificial-intelligence/how-google-self-driving-car-works> (2011).
- [2] D. Balis, A. Papayannis, E. Galani, F. Marengo, V. Santacesaria, E. Hamonou, P. Chazette, I. Ziomas, and C. Zerefos, “Tropospheric LIDAR aerosol measurements and sun photometric observations at Thessaloniki, Greece,” *Atmos. Environ.*, **34**(6), 925{932 (2000).
- [3] C. W. J. Oh, E. Tangdiongga, and A. M. J. T. Koonen, “42.8 Gbit / s Indoor Optical Wireless Communication with 2 - Dimensional Optical Beam - steering,” *Opt. Fiber Commun. (OFC)*, M2F.3 (2015).
- [4] “A Brief introduction to LiDAR Technology and its Market Applications” <https://leddartech.com/why-lidar/>
- [5] Mial E. Warren, David Podva, Preethi Dacha, Matthew K. Block, Christopher J. Helms, “Low-divergence high-power VCSEL arrays for lidar application”
- [6] Norbert Druml, Ievgeniia Maksymova, Thomas Thurner, Diederik van Lierop, Marcus Hennecks and Andreas Foroutan, “1D MEMS Micro-Scanning LiDAR”
- [7] Motaz Khader, Samir Cherian, “An Introduction to Automotive LIDAR”, Texas Instruments Incorporated (2018).
- [8] 池上徹彦, 土屋治彦, 三上修, “半導体フォトニクス工学,” コロナ社(1995).
- [9] P. R. A. Binetti, C. Althouse, M. L. Masanovic, H. P. M. M. Ambrosius, L. A. Johansson, and L. A. Coldren, “Two-Dimensional Optical Beam Steering With InP-Based Photonic Integrated Circuits,” *IEEE J. Sel. Top. Quantum Electron.*, **19**(4), 6100212 (2013).
- [10] 小松憲人, “高速イメージング応用に向けた InP 光集積フェーズドアレイに関する研究,” 東京大学修士論文(2017).
- [11] S. R. _sehni_c, G. A. Evans, T. M. Chou, J. B. Kirk, J. N. Walpole, J. P. Donnelly, C. T. Harris, and L. J. Missaggia, “Single frequency 1550-nm AlGaInAs-InP tapered high-power laser with a distributed Bragg reector,” *IEEE Photonics Technol. Lett.*, **14**(7), 890{892(2002).
- [12] J. W. Raring and L. A. Coldren, “40-Gb/s widely tunable transceivers” *IEEE Journal of Selected Topics in Quantum Electronics*, vol. 13, no. 1, pp. 3-14, Jan./Feb. 2007.
- [13] Hongwei Zhao, “High Power Indium Phosphide Photonic Integrated Circuits” *IEEE Journal of Selected Topics in Quantum Electronics* (2019)
- [14] E. Skogen, “Integration of high-saturation-power active regions using quantum-well intermixing and offset-quantum-well regrowth”
- [15] Ibrahim Murat Soganci, “Integrated Phased-Array Photonic Switches for Ultra-Large-Capacity Optical Packet Routing”, a doctor course dissertation of the University of Tokyo (2010).

- [16] Paul W. Juodawlkis, "High-Power, Low-Noise 1.5- μm Slab-Coupled Optical Waveguide (SCOW) Emitters: Physics, Devices, and Applications", IEEE JOURNAL OF SELECTED TOPICS IN QUANTUM ELECTRONICS, VOL. 17, NO. 6, NOVEMBER/DECEMBER 2011
- [17] B. E. A. Saleh, M. C. Teich, "基本光光学 1," 森北出版(2006).
- [18] Aloysius Wehr, Uwe Lohr, "Airborne laser scanning-an introduction and overview", ISPRS Journal of Photogrammetry & Remote Sensing 54 (1999).
- [19] Markku Koskinen, Juha Tapio Kostamovaara, Risto A. Myllylae, "Comparison of continuous-wave and pulsed time-of-flight laser range-finding techniques", Proc. SPIE 1614, Optics, illumination, and Image Sensing for Machine Vision VI, (1 March 1992).
- [20] Santiago Royo and Maria Ballesta, "An overview of imaging lidar sensors for autonomous vehicles", Centre for Sensor, Instrumentation and systems Development, Universitat Politècnica de Catalunya
- [21] Y. P. Varshni, "Temperature dependence of the energy gap in semiconductors," *Physica*, **34**(1), 149{154 (1967).
- [22] B. R. Bennett, R. A. Soref, and J. A. Del Alamo, "Carrier-Induced Change in Refractive Index of InP, GaAs, and InGaAsP," IEEE J. Quantum Electron., 26(1), 113{122 (1990).
- [23] 田中信介, "歪多重量子井戸半導体光増幅器の高性能化に関する研究", 2013、博士論文
- [24] Connelly, Michael J. "Wideband semiconductor optical amplifier steady-state numerical model." (2001).
- [25] Coldren, L. A., Corzine, S. W., & Mashanovitch, M. L. Mashanovitch. "Diode lasers and photonic integrated circuits". Second Edition. John Wiley & Sons, 2012.
- [26] Cheng, N., & Kazovsky, L. G. "Implications of injection current and optical input power on the performance of reflective semiconductor optical amplifiers." Integrated Optoelectronic Devices 2007. International Society for Optics and Photonics, 2007.
- [27] Zhan Wenhui, "Optical Design of Self-seeded Reflective Semiconductor Optical Amplifier for Low-cost Wavelength Division Multiplexed Passive Optical Network Applications", Master thesis, the University of Tokyo, 2016.
- [28] Agrawal, G. P., & Olsson, N. A. "Self-phase modulation and spectral broadening of optical pulses in semiconductor laser amplifiers." Quantum Electronics, IEEE Journal of 25.11 (1989): 2297-2306.
- [29] Agrawal, G. P. "Fiber-optic communication systems." Third Edition, John Wiley & Sons, Inc. (2002).
- [30] Jay A. Overbeck "Required energy for a laser radar system incorporating a fiber amplifier or an avalanche photodiode", applied optics, 1995
- [31] Markus A. Fredell "Sub-nanometer band pass coatings for LIDAR and astronomy", Proc. of SPIE Vol. 9612
- [32] Thomas D Rahmlow "Ultra-narrow Bandpass filters for infrared applications with improved

angle of incidence performance”, Proc. of SPIE Vol. 9822

[33] 馬場俊彦, シリコンフォトニクス技術を用いたスローライト LiDAR の検討, 日本学術振興会第 130 委員会, no. 3, 2017.

[34] Paul W. Juodawlkis, “Packaged 1.5- μm Quantum-Well SOA With 0.8-W Output Power and 5.5-dB Noise Figure”, IEEE JOURNAL OF SELECTED TOPICS

[35] 伊藤まいこ, “高効率偏波制御器に向けた InGaAsP 歪量子井戸型光位相シフトの設計と試作,” 東京大学卒業論文(2019).

[36] M. Zaitse, T. Tanemura, A. Higo, and Y. Nakano, “ Experimental demonstration of self-aligned InP/InGaAsP polarization converter for polarization multiplexed photonic integrated circuits, ” Opt. Express, 21(6), 6910{6918 (2013).

[37] 菅沼貴博, “三次元偏波変調による大容量通信に向けた光集積ストークスペクトル受信回路に関する研究,” 東京大学修士論文(2019).

[38] S. Adachi and H. Kawaguchi, “ Chemical etching characteristics of (001) InP, ” J. Electrochem. Soc., 128(6), 1342{1349 (1981).

[39] Bernhard Semlitsch, “ Advanced Ray Tracing Techniques for Simulation of Thermal Radiation in Fluids “, University of Cambridge, 2010.

[40] Basil W. Haki and Thomas L. Paoli, “ Gain spectra in GaAs double-heterostructure injection lasers”, Bell Laboratories, 1974.

List of Publications

[1] 小野塚章太, 河野佑亮, 種村拓夫, 中野義昭, “光フェーズドアレイ素子の高出力化に向けた半導体光増幅器の試作”, 電子情報通信学会光エレクトロニクス研究会, 湯河原, 2018年4月

[2] 小野塚章太, 福井太一郎, 種村拓夫, 中野義昭, “Design of Semiconductor Optical Amplifier for High Power Optical Phased Array”, Photonic device workshop, 東京, 2019年12月

Acknowledgements

本研究を進めるに当たり、多くの方々のご協力を賜りました。この場を借りて深く感謝申し上げます。

指導教官である中野義昭教授からは、研究室ミーティングにて半導体光増幅器などに関する有益な助言を多く賜りました。また、本研究を行うための環境を提供して頂いたほか、世界中から留学生を積極的に受け入れることによって多様な価値観に触れられる機会を与えて下さりました。

種村拓夫准教授からは、私が学部生として本研究に取り組み始めて以来、3年間にわたり手厚いご指導を頂きました。理論と直観の両側面からの鋭いご指摘を数多く頂いただけでなく、対外発表の機会などを設けて下さりました。また、発表の仕方や予稿の書き方についても多くのことを学ばせていただきました。

杉山正和教授および渡辺健太郎特任講師からは、主に研究室のミーティングの場で有機金属気相成長法に関して長年の研究を通じて得た深い知見に基づいた鋭いご指摘を賜りました。

佐藤正寛助教には、主に研究室の飲み会で個人的な相談に乗っていただきました。

ヤンワチラクーン・ワラコーン特任助教及びソダーバンル・ハサネット特任助教からは四元混晶の多重量子井戸の結晶成長の際に、装置の使用方法やレシピの書き方そして成長したサンプルの測定方法などをご指導いただきました。

学術支援職員の加藤豪作氏には、実験装置の維持管理をはじめとして、幾度となくお力添えを賜りました。特に MOVPE 装置関連では大変お世話になりました。

唐睿氏そして黄祥鴻氏は将来の進路や私生活に関する相談に何度も応じて下さりました。

周鵬氏からは半導体光増幅器の増幅特性を計算するプログラムに関してのアドバイスを賜りました。

徐皓氏は、研究室の飲み会で氏がこれまでの人生で体験した経験を数多くお話して下さい、私の知見を広げて下さりました。

今関裕貴氏には、結晶成長したサンプルの表面状態を計測する実験装置の使用方法を教えて頂きました。

イマラ・サマル・アラー氏には普段の研究室での生活だけでなく、私生活でもお世話になりました。氏が話して下さいた話題は大変興味深い内容が多く、私の知見を広げて下さりました。また、研究室内のミーティングが円滑に進むよう司会を務めてくださりました。

石村昇太氏は、将来の進路に関する相談に応じて下さりました。また、社会人として忙しい日々を過ごす傍らに博士号取得を目指す姿勢には大変感銘を受けました。

モンゴル・バトプレフ氏は、これまでの人生で体験した経験を数多くお話して下さい、私の知見を広げて下さりました。また、研究室内のミーティングが円滑に進むよう司会を

務めてくださりました。

弊研に在籍していたカズイ・モヒユディン・アタルディン氏、ゴッシュ・サミール氏、張家琦氏、肖火習氏、小林竜馬氏、西本昌哉氏、福田将治氏、山下大之氏、キム・ボラム氏、小杉優地氏、菅一輝氏、中田達也氏には半導体プロセスの流れや半導体プロセス装置の使用方法に関して主にご指導いただきました。

一学年上の先輩方である王宇光氏、大川幸祐氏、河野佑亮氏、菅沼貴博氏、丸山裕晃氏、渡邊充洋氏からは、半導体プロセス装置の使用方法や光学系の組み方に関して主にご指導いただきました。また、身近な先輩として研究生活を支援していただきました。

同級生である浅見明太氏、小笠原誠氏、岡田哲明氏、田之村亮汰氏、福井太一郎氏、福谷貴史氏、マシア・テオフィル星二郎氏には、学部時代から研究に関して幾度となくご協力を頂いただけでなく、充実した研究生活を送る上でかけがえのない存在でした。

一学年後輩である伊藤まいこ氏、梅崎敏和氏、沈昊哉氏、土屋里穂子氏、日野眞生氏、宮崎俊輝氏、劉沁培氏は、研究室での生活を有意義に過ごす上で欠かせない存在でした。

二学年後輩である小野寺文太氏、相馬豪氏、藤澤燦氏、町拓郎氏、横田莉子氏は私のたわいもない話によく付き合ってくださいました。

その他、ここには名前をあげることができなかった皆様にも深く御礼申し上げます。本研究は皆さまのお力を借りることなしには成立しないものでした。

最後に、私の生活を支えてくださった家族、友人をはじめとする全ての方々に深く感謝いたします。

拙い言葉を並べましたが、今の私を形作った全てに感謝しつつ、これを以て謝辞に代えさせていただきます。

2020年1月
小野塚章太